Journal of Computational Physics 556 (2026) 114812

Contents lists available at ScienceDirect

Journal of Computational Physics

journal homepage: www.elsevier.com/locate/jcp

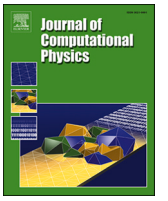

Efficient computation of the forcing term in Enskog Vlasov equation

Zuoxu Li [a,b], Shaokang Li [a], Tianbai Xiao [a,b], Yonghao Zhang [a,b,*]

[a] Centre for Interdisciplinary Research in Fluids, Institute of Mechanics, Chinese Academy of Sciences, Beijing, China
[b] School of Engineering Science, University of Chinese Academy of Sciences, Beijing, China

ARTICLE INFO

Keywords:
Enskog Vlasov equation
High-order lattice Boltzmann method
Hermite expansion
Non-equilibrium evaporation

ABSTRACT

The Enskog-Vlasov (EV) equation extends the Enskog model to describe the non-equilibrium transport of dense gases and liquids. It captures non-equilibrium phase transitions and rarefaction effects that are beyond the capabilities of the continuum fluid mechanics. A major computational challenge in solving the EV equation lies in the accurate and efficient evaluation of the forcing term, e.g., long-range intermolecular interactions and external body forces, which can significantly influence phase changes and flow behavior, especially near surfaces.

In this work, we propose a method that utilizes Hermite polynomials to reformulate the EV forcing term by expanding the molecular velocity distribution function in a locally shifted-and-scaled velocity space. This approach recovers the exact forcing term for near-equilibrium flows and computes non-equilibrium corrections with far fewer discrete velocities and larger time steps compared to conventional finite difference methods. As a result, the computational cost is greatly reduced without sacrificing simulation accuracy. To further simplify implementation, we present a component-wise derivation of the Hermite expansion, avoiding complex tensorial manipulations and reducing computational burden. The efficiency and accuracy of the proposed method are validated through numerical simulations of non-equilibrium transport of surface-confined dense fluids at the nanoscale and of non-equilibrium evaporative flows. This method enables efficient molecular kinetic simulations of non-equilibrium transport of dense fluids, particularly when accounting for phase changes and surface confinement at the nano-scale.

1. Introduction

Non-equilibrium transport of dense fluids is ubiquitous in nature and industrial processes, e.g., high-power electronics cooling [1–3] and micro-electromechanical devices [4]. The non-equilibrium phenomena including the temperature jump at the liquid-vapour interface cannot be captured by the conventional continuum theory. Meanwhile molecular dynamics (MD) simulations are prohibitively expensive to describe such phenomena [5].

The Enskog-Vlasov (EV) kinetic equation has emerged as a powerful theoretical framework addressing non-equilibrium transport of dense fluids, augmenting the Boltzmann equation with an Enskog collision operator for excluded-volume effect and a Vlasov mean-field forcing term for long-range van der Waals attractions [6–8]. Therefore, the dense fluid effects including spontaneous liquid-vapor separation, capillary phenomena, which are inaccessible to hydrodynamics, can be captured with the molecular velocity distribution

* Corresponding author.
E-mail address: yonghao.zhang@imech.ac.cn (Y. Zhang).

https://doi.org/10.1016/j.jcp.2026.114812
Received 14 September 2025; Received in revised form 15 February 2026; Accepted 23 February 2026
Available online 26 February 2026

function $f(\mathbf{r},\mathbf{v},t)$ evolving under streaming and non-local collisions, and a self-consistent body force derived from an intermolecular potential $\phi(\mathbf{r})$ [9].

Despite its physical fidelity, the non-local Enskog integral requires high-order quadratures, and the Vlasov forcing term demands evaluation of the velocity-space gradients over an unbounded domain, resulting in high computational costs [10]. While various solution strategies exist, e.g., statistical particle methods [11,12], moment closures [9,13], Fokker-Planck-Poisson approximations [14], and spectral discretizations [15,16], significant progress has been made in simplifying the collision operator of the EV equation using the classic relaxation time approach [8,17–19]. The resulting Enskog-Vlasov-Shakhov model can significantly reduce the computational cost, which has an adjustable Prandtl number and correct transport coefficients, and can also be calibrated for specific intermolecular potentials. It has recently been validated for non-equilibrium evaporative flows [20,21]. However, computational efficiency is still hindered by a lack of efficient scheme for the Vlasov forcing term.

The difficulty in efficiently solving EV-type models with a discrete velocity method (DVM) arises from the numerical treatment of the forcing term. The original EV equation and its kinetic variants can be expressed as:

$$\partial_t f + \boldsymbol{\xi}\cdot\nabla_{\mathbf{r}} f + (\mathbf{F}_{\text{att}} + \mathbf{F}_{\text{ext}})\cdot\nabla_{\boldsymbol{\xi}} f = C[f], \tag{1}$$

where $\mathbf{F}_{\text{att}}$ represents an attractive intermolecular force, $\mathbf{F}_{\text{ext}}$ denotes an external body force (e.g., gravitational force, electromagnetic force), and $C[f]$ is a collision operator. For non-equilibrium flows, the forcing term contributes to not only momentum but also higher-order velocity moments, thereby influences non-equilibrium heat fluxes and other high order moments [22–25]. In addition, for EV-type models, the attractive force $\mathbf{F}_{\text{att}}$ drives molecules to form liquid-vapor interfaces and shape, density variation, resulting in surface tension that dominates interfacial dynamics [20,26]. Any inaccuracy in evaluating $(\mathbf{F}_{\text{att}} + \mathbf{F}_{\text{ext}})\cdot\nabla_{\boldsymbol{\xi}} f$ can directly affect the computed mass, momentum, and energy flux.

The numerical difficulty arises from approximating $\nabla_{\boldsymbol{\xi}} f$ over an unbounded velocity domain. The existing methods for evaluating the forcing term can be broadly classified into four categories: equilibrium distribution approximations, Hermite expansions, finite-difference discretizations, and Fourier spectral methods. By separating non-equilibrium and equilibrium components, i.e., $f = f^{\text{eq}} + f^{\text{neq}}$, $\nabla_{\boldsymbol{\xi}} f = \nabla_{\boldsymbol{\xi}} f^{\text{eq}} + \nabla_{\boldsymbol{\xi}} f^{\text{neq}}$, one finds that, for near equilibrium flows, $\nabla_{\boldsymbol{\xi}} f \approx \nabla_{\boldsymbol{\xi}} f^{\text{eq}} = -\frac{\boldsymbol{\xi}-\mathbf{u}}{RT} f^{\text{eq}}$, which admits a closed-form expression with high efficiency and accuracy [27]. However, this analytic form neglects the non-equilibrium gradient $\nabla_{\boldsymbol{\xi}} f^{\text{neq}}$, essential for capturing highly non-equilibrium transport phenomena. An alternative method commonly applied in the lattice Boltzmann method is to expand the distribution function into the Hermite polynomial series of molecular velocity $\boldsymbol{\xi}$ as $f \approx (2\pi)^{-D/2}\exp\left(-|\boldsymbol{\xi}|^2\right)\sum_{n=0}^{N}\frac{1}{n!}\mathbf{a}^{(n)} : \mathcal{H}^{(n)}(\boldsymbol{\xi})$, recovering the mass and momentum equations at second order [28] and the energy equation at third order [29–31]. But current lattice Boltzmann implementations are restricted to continuous flows [32]. For non-equilibrium flows, the existing methods rely on the finite-difference approximations requiring very fine velocity discretization and time steps [20,33] or the Fourier spectral transform [15], resulting in high memory consumption and computational cost. Consequently, none of the existing methods can simultaneously provide accuracy, efficiency, and robustness in simulating non-equilibrium flows, which demands an improved forcing-term algorithm.

To address this issue, we utilize Hermite expansion in the locally shifted-and-scaled velocity space defined by $\mathbf{v} = (\boldsymbol{\xi} - \mathbf{u})/\sqrt{RT}$, where $\mathbf{u}$ and T are the local macroscopic velocity and temperature [34]. Unlike the traditional lattice Boltzmann method that expands f around the molecular velocity $\boldsymbol{\xi}$ with the weight $\omega(\boldsymbol{\xi}) = (2\pi)^{-D/2}\exp\left(-|\boldsymbol{\xi}|^2\right)$, our approach uses the local Maxwellian to define the weight in the velocity space, i.e., $\omega(\mathbf{v}) = f^{\text{eq}}(RT)^{D/2}/\rho = (2\pi)^{-D/2}\exp\left(-|\mathbf{v}|^2/2\right)$. As a result, the zeroth-order Hermite coefficient coincides exactly with f^{eq}, and higher-order coefficients converge at a spectral rate to capture non-equilibrium deviations. By coupling this expansion with a shifted-and-scaled Gaussian-Hermite quadrature (GHQ) [35–37], we will reduce the required number of discrete velocities by one to two orders of magnitude and enable the time step up to ten times larger than the finite difference schemes, without compromising numerical accuracy. Moreover, to ease implementation of high-order expansions, we will derive an explicit component-wise formulation for the Hermite basis functions and coefficients, which directly yields expressions for every directional component to avoid manipulation of full tensors. This scheme can automatically generate the expanded terms at an arbitrary order, greatly streamlining implementation and code maintenance without any additional cost. Although motivated by the Enskog-Vlasov-Shakhov equation, this scheme can be applied to the generic kinetic models with body forcing term, e.g., gravitational, electrostatic, electromagnetic, and inertial forces, thus enabling efficient and high-fidelity simulations of a broad range of non-equilibrium flows.

The rest of this paper is organized as follows. Section 2 briefly summarizes the Enskog-Vlasov-Shakhov equation. Section 3 details the scaled-velocity Hermite expansion for the forcing term. Section 4 constructs the shifted-and-scaled GHQ, and Section 5 presents the non-dimensionalization process. Section 6 provides numerical validation and analysis, with the conclusions drawn in Section 7.

2. Enskog-Vlasov-Shakhov equation

In dense fluids, intermolecular interactions, including short-range repulsive forces and long-range attractive forces, play an important role in phase transitions [38,39] and interfacial dynamics [14]. To account for these interactions, the kinetic models for both dilute and dense gases can be derived from the BBGKY hierarchy [27]. For dense gases, the molecular chaos assumption does not hold, and the distribution functions of molecules are not independent of each other. Therefore, the evolution equation of the single-particle distribution function $f(\mathbf{r},\boldsymbol{\xi},t)$ involves the two-particle joint distribution function $f^{(2)}(\mathbf{r},\boldsymbol{\xi},\mathbf{r}_1,\boldsymbol{\xi}_1,t)$:

$$\frac{\partial f}{\partial t} + \boldsymbol{\xi}\cdot\nabla f + \mathbf{F}_{\text{ext}}\cdot\nabla_{\boldsymbol{\xi}} f = \int\int \frac{\partial f^{(2)}}{\partial \boldsymbol{\xi}}\cdot\nabla\phi(\mathbf{r},\mathbf{r}_1)d\boldsymbol{\xi}_1 d\mathbf{r}_1, \tag{2}$$

where $\phi(\mathbf{r},\mathbf{r}_1)$ is the intermolecular potential. To further simplify the model, it is necessary to close the equation for $f^{(2)}$. For dilute gases, the distribution functions can be considered not correlated, i.e., $f^{(2)} \approx f(\mathbf{r},\boldsymbol{\xi},t)f(\mathbf{r}_1,\boldsymbol{\xi}_1,t)$. For dense fluids, the radial distribution

function $\chi(\rho)$ is introduced to describe the increase in collision frequency. Therefore, the two-particle distribution function can be approximated as: $f^{(2)} \approx \chi\left(\frac{\mathbf{r}+\mathbf{r}_1}{2}\right) f(\mathbf{r},\boldsymbol{\xi},t) f(\mathbf{r}_1,\boldsymbol{\xi}_1,t)$ [40].

In addition, molecular interactions may be separated into the short-range and long-range molecular interactions, so the BBGKY hierarchy can be simplified to the Enskog-Vlasov equation [6], i.e.,

$$\frac{\partial f}{\partial t} + \boldsymbol{\xi}\cdot\nabla f + (\mathbf{F}_{\text{ext}} + \mathbf{F}_{\text{att}})\cdot\nabla_{\xi} f = J_E, \tag{3}$$

where J_E is the Enskog collision term,

$$J_E(f,f) = \sigma^2 \int \left[\chi(\mathbf{r}+\frac{1}{2}\sigma\mathbf{k}) f(\mathbf{r},\boldsymbol{\xi}') f(\mathbf{r}+\sigma\mathbf{k},\boldsymbol{\xi}_1') - \chi(\mathbf{r}-\frac{1}{2}\sigma\mathbf{k}) f(\mathbf{r},\boldsymbol{\xi}) f(\mathbf{r}-\sigma\mathbf{k},\boldsymbol{\xi}_1)\right] \mathbf{g}\cdot\mathbf{k}\, d\boldsymbol{\xi}_1\, d\mathbf{k}, \tag{4}$$

σ is the molecular diameter, $\mathbf{g} = \boldsymbol{\xi}_1 - \boldsymbol{\xi}$ is the relative velocity between two particles, $\mathbf{k} = (\mathbf{r}_1 - \mathbf{r})/|\mathbf{r}_1 - \mathbf{r}|$ is the unit vector specifying the relative position between two particles, and $\boldsymbol{\xi}'$ and $\boldsymbol{\xi}_1'$ are the post-collision velocities. The long-range attractive force between molecules $\mathbf{F}_{\text{att}}$ can be expressed as

$$\mathbf{F}_{\text{att}} = -\int_{|\mathbf{r}|>\sigma} n(\mathbf{r}+\mathbf{r}')\nabla\phi_{\text{att}}(|\mathbf{r}'|)\, d\mathbf{r}', \tag{5}$$

where $\phi_{\text{att}}(|\mathbf{r}'|)$ is the long-range attractive potential. In this paper, we use the Sutherland potential,

$$\phi_{\text{att}} = -\epsilon_p\left(\frac{\sigma}{r}\right)^6, \quad |\mathbf{r}| > \sigma, \tag{6}$$

where ϵ_p is the depth of the potential well. As shown, the long-range attractive force between molecules is approximated as a body force, while the short-range interactions are included in the collision term, considering the effect of molecular volume.

Expanding the Enskog collision term at the spatial location $\mathbf{r}$ using a second-order Taylor series and approximating the gradient of f in the physical space with the equilibrium distribution function $f^{(0)}$, we obtain the Enskog-Vlasov-Shakhov model [17–19,27],

$$J_E(f,f) \approx \chi J^{(0)} + J^{(1)} + J^{(2)}, \tag{7}$$

where $J^{(0)}$ describes the Boltzmann collision term for dilute gases, which can be further simplified using the Shakhov model. The terms $J^{(1)}$ and $J^{(2)}$ account for the dense fluid effects as the fluid density increases. The expression for $J^{(0)}$ is

$$J^{(0)} = -\frac{1}{\tau}\left[f - f^{(0)}\left(1 + (1-Pr)\frac{\mathbf{c}\cdot\mathbf{q}}{5p_0RT}\left(\frac{c^2}{RT} - 5\right)\right)\right], \tag{8}$$

and the first-order term $J^{(1)}$ is

$$J^{(1)} = -\rho b\chi f^{(0)}\left[\mathbf{c}\cdot\left(\nabla\ln(\rho^2\chi T) + \frac{3}{5}\left(\frac{c^2}{2RT} - \frac{5}{2}\right)\nabla\ln T + \frac{2}{5}\left(\frac{\mathbf{c}^2}{RT} : \nabla\mathbf{u} + \left(\frac{c^2}{2RT} - \frac{5}{2}\right)\nabla\cdot\mathbf{u}\right)\right)\right]. \tag{9}$$

The second-order term $J^{(2)}$ is

$$J^{(2)} = \nabla\cdot\left(f^{(0)}\frac{\mu_B}{p_0}(\nabla\cdot\mathbf{u})\left(\frac{c^2}{2RT} - \frac{3}{2}\right)\mathbf{c}\right), \tag{10}$$

where ρ, $\mathbf{u}$, and T represent density, macroscopic velocity, and temperature of the fluid, respectively, with their relation to the distribution function given by

$$\int f\{1, \boldsymbol{\xi}, c^2/2\} d\boldsymbol{\xi} = \{\rho, \rho\mathbf{u}, \frac{3}{2}\rho RT\}. \tag{11}$$

Here, $\mathbf{c} = \boldsymbol{\xi} - \mathbf{u}$, $\mathbf{q} = \frac{1}{2}\int f c^2 \mathbf{c} d\boldsymbol{\xi}$ is the heat flux vector, τ is the relaxation time, Pr is the Prandtl number, $p_0 = \rho RT$ is the ideal gas pressure, R is the gas constant, $b = \frac{2\pi\sigma^3}{3m}$, m is the molecular mass, σ is the molecular diameter, μ_B is the bulk viscosity, and $f^{(0)}$ is the equilibrium distribution function, given by

$$f^{(0)} = \frac{\rho}{(2\pi RT)^{3/2}}\exp\left(-\frac{c^2}{2RT}\right). \tag{12}$$

Through the Chapman-Enskog expansion [19], the macroscopic hydrodynamic equations in the continuum limit can be derived as follows,

$$\frac{\partial\rho}{\partial t} + \nabla\cdot(\rho\mathbf{u}) = 0, \tag{13}$$

$$\rho\left(\frac{\partial\mathbf{u}}{\partial t} + \mathbf{u}\cdot\nabla\mathbf{u}\right) = -\nabla\left((1+b\rho\chi)p_0 - \mu_B(\nabla\cdot\mathbf{u})\right) + 2\nabla\cdot(\mu_s S) + \rho(\mathbf{F}_{\text{att}} + \mathbf{F}_{\text{ext}}), \tag{14}$$

$$\frac{\partial}{\partial t}(\rho E) + \nabla\cdot(\rho E\mathbf{u}) = -\nabla\cdot\left[\left((1+b\rho\chi)p_0 - \mu_B(\nabla\cdot\mathbf{u})\right)\mathbf{u}\right] + 2\nabla\cdot(\mu_s S\cdot\mathbf{u}) + \rho(\mathbf{F}_{\text{att}} + \mathbf{F}_{\text{ext}})\cdot\mathbf{u}, \tag{15}$$

where $E = \frac{3RT+u^2}{2}$ is the total energy per unit mass, μ_s is the shear viscosity, and S is the strain rate tensor, i.e.,

$$S = \frac{1}{2}\left[\nabla\mathbf{u} + (\nabla\mathbf{u})^T\right] - \frac{1}{3}(\nabla\cdot\mathbf{u})\boldsymbol{\delta}, \tag{16}$$

where $\boldsymbol{\delta}$ is the unit tensor. The relaxation time τ and Prandtl number Pr can be determined by

$$\tau = \frac{\mu_s}{p_0}\frac{1}{1+0.4\rho b\chi}, \quad Pr = \frac{5R}{2}\frac{1+0.6\rho b\chi}{1+0.4\rho b\chi}\frac{\mu_s}{\lambda}, \tag{17}$$

where the shear viscosity μ_s, bulk viscosity μ_B, and thermal conductivity λ are related to the intermolecular interactions. Shan et al. [19] discussed the effects of different intermolecular potentials, such as the Lennard-Jones potential and hard-sphere potential, on the transport coefficients. In this work, we use the hard-sphere potential, whose viscosity and heat conductivity are

$$\mu_s = \frac{1}{\chi}\left(1+\frac{2}{5}\rho b\chi\right)^2\mu^* + \frac{3}{5}\mu_B, \quad \mu_B = (\rho b)^2\chi\mu^*, \quad Pr = \frac{2}{3}\frac{\left(1+\frac{2}{5}\rho b\chi\right)^2 + \frac{3}{5}(\rho b\chi)^2}{\left(1+\frac{3}{5}\rho b\chi\right)^2 + \frac{2}{5}(\rho b\chi)^2}, \tag{18}$$

where $\mu^* = \frac{5}{16\sigma^2}\sqrt{\frac{mk_bT}{\pi}}$ is the shear viscosity of a dilute hard-sphere gas.

To explain the effect of the attractive force $\mathbf{F}_{\text{att}}$ on equation of state and surface tension, we can further simplify the attractive force $\mathbf{F}_{\text{att}}$ by expanding the density in the physical space using a Taylor series and then obtain:

$$\mathbf{F}_{\text{att}} \approx 2a\nabla\rho + \kappa\nabla(\nabla\cdot\nabla)\rho, \tag{19}$$

where the coefficients a and κ are computed as integration of the intermolecular potential [41], i.e.,

$$a = \frac{1}{6}\int_{r>\sigma}\frac{d\phi(r)}{dr}rd\mathbf{r} \quad \text{with } \kappa = \frac{1}{30}\int_{r>\sigma}\frac{d\phi(r)}{dr}r^3d\mathbf{r}. \tag{20}$$

The first term, $2a\nabla\rho$, contributes to the non-ideal pressure gradient arising from the attractive tail of the potential, thereby modifying the equation of state. The second term, $\kappa\nabla(\nabla\cdot\nabla)\rho$, represents a capillary force that emerges due to density inhomogeneities within the fluid. The surface tension coefficient can be quantitatively evaluated as $\gamma = \kappa\int_{-\infty}^{+\infty}\left(\frac{d\rho}{dx}\right)^2dx$ [19,41]. For the Sutherland potential, $a = \frac{4\pi}{3}\sigma^3\epsilon_p$ and $\kappa = \frac{4\pi}{5}\sigma^5\epsilon_p$.

Substituting Eq. 19 into Eq. 15, we recover the pressure as $p = p_0(1+b\rho\chi) - a\rho^2$, which is the equation of state for a non-ideal gas. By choosing a different form of χ, we can derive different equation of state. In this work, we choose $\chi = \frac{1-0.5\eta}{(1-\eta)^3}$, where $\eta = 0.25b\rho$, to obtain the Carnahan-Starling-van der Waals equation of state [42]:

$$p = p_0\frac{(1+\eta+\eta^2-\eta^3)}{(1-\eta)^3} - a\rho^2. \tag{21}$$

3. Modelling the forcing term

To describe the effect of external force $\mathbf{F}_{\text{ext}}$ and long-range intermolecular attraction $\mathbf{F}_{\text{att}}$ on the flow, it is crucial to construct an accurate and efficient scheme to compute the gradient of the distribution function in the velocity space, i.e., $\nabla_\xi f$. Following Grad [34], the distribution function is expanded as an N_{th} order Hermite polynomial series,

$$f \approx f_N = \omega(\upsilon)\sum_{n=0}^{N}\frac{1}{n!}\mathbf{d}^{(n)}(\mathbf{x},t) : \mathcal{H}^{(n)}(\mathbf{v}), \tag{22}$$

where $\mathbf{v} = (\boldsymbol{\xi}-\mathbf{u})/\sqrt{RT}$ is the rescaled molecular velocity based on the local macroscopic fluid velocity and temperature, ':' stands for full contraction between two tensors, $\mathcal{H}^{(n)}(\mathbf{v})$ is the n_{th} tensorial Hermite polynomial, $\omega(\upsilon) \equiv \frac{1}{\sqrt{2\pi}^3}\exp(-\upsilon^2/2) = \frac{\sqrt{RT}^3}{\rho}f^{(0)}$ is the weighting function, and the central moments of the distribution function $\mathbf{d}^{(n)}$ are given by

$$\mathbf{d}^{(n)} = \int f\mathcal{H}^{(n)}(\mathbf{v})\,d\mathbf{v} = \frac{\rho}{\sqrt{RT}^3}\frac{1}{\rho}\int f\mathcal{H}^{(n)}(\mathbf{v})\,d\boldsymbol{\xi}. \tag{23}$$

$\mathcal{H}^{(n)}(\mathbf{v})$ and $\omega(\upsilon)$ are related by

$$\mathcal{H}^{(n)}(\mathbf{v}) = \frac{(-1)^n}{\omega(\upsilon)}\nabla^{(n)}\omega(\upsilon). \tag{24}$$

Consequently, the recurrence formula of the Hermite polynomials [43] can be written as

$$\mathcal{H}_i^{(n+1)}(\mathbf{v}) = \mathbf{v}_i\mathcal{H}^{(n)}(\mathbf{v}) - n\boldsymbol{\delta}_i\mathcal{H}^{(n-1)}. \tag{25}$$

The leading Hermite polynomials can be obtained as

$$\mathcal{H}^{(0)}(\mathbf{v}) = 1, \tag{26a}$$

$$\mathcal{H}^{(1)}(\mathbf{v}) = \mathbf{v}, \tag{26b}$$

$$\mathcal{H}^{(2)}(\mathbf{v}) = \mathbf{v}^2 - \boldsymbol{\delta}, \tag{26c}$$

$$\mathcal{H}^{(3)}(\mathbf{v}) = \mathbf{v}^3 - 3\mathbf{v}\boldsymbol{\delta}, \tag{26d}$$

$$\mathcal{H}^{(4)}(\mathbf{v}) = \mathbf{v}^4 - 6\mathbf{v}^2\boldsymbol{\delta} + 3\boldsymbol{\delta}^2, \tag{26e}$$

$$\cdots, \tag{26f}$$

and the corresponding central moments are

$$\mathbf{d}^{(0)} = \frac{\rho}{\sqrt{RT}^3}, \tag{27a}$$

$$\mathbf{d}^{(1)} = \mathbf{0}, \tag{27b}$$

$$\mathbf{d}^{(2)} = -\frac{\rho}{\sqrt{RT}^3}\frac{\boldsymbol{\zeta}}{p_0}, \tag{27c}$$

$$\mathbf{d}^{(3)} = \frac{\rho}{\sqrt{RT}^3}\frac{\mathbf{Q}}{p_0\sqrt{RT}}, \tag{27d}$$

$$\mathbf{d}^{(4)} = \frac{\rho}{\sqrt{RT}^3}\left(\frac{\mathbf{M}}{p_0 RT} + \frac{6\boldsymbol{\zeta}\boldsymbol{\delta}}{p_0} - 3\boldsymbol{\delta}^2\right) \tag{27e}$$

$$\cdots, \tag{27f}$$

where $\boldsymbol{\delta}$ is the unit tensor, $\boldsymbol{\zeta} = \int f(RT\boldsymbol{\delta} - \mathbf{c}^2)\,d\boldsymbol{\xi}$ is the shear stress, $\mathbf{Q} = \int f\mathbf{c}^3\,d\boldsymbol{\xi}$ is the heat transfer tensor, related to the heat flux vector by $q_i = \frac{1}{2}Q_{kki}$, and $\mathbf{M} = \int f\mathbf{c}^4\,d\boldsymbol{\xi}$, which influences the evolution of heat flux in the moment equations. All tensors and tensor products above are symmetric. For example, the third-order tensor $\mathbf{c}^3$ denotes the symmetric product $c_i c_j c_k$, and the symmetrized tensor product $\mathbf{v}\boldsymbol{\delta}$ is defined by $\mathbf{v}\boldsymbol{\delta} = \frac{1}{3}(v_i\delta_{jk} + v_j\delta_{ik} + v_k\delta_{ij})$ [43,44].

By substituting the expanded distribution function and performing some algebraic and differential calculations, we obtain

$$\begin{aligned}\mathbf{F}\cdot\nabla_{\xi} f \approx \frac{1}{\sqrt{RT}}\nabla_v f_N &= \frac{1}{\sqrt{RT}}\mathbf{F}\cdot\nabla_v\left(\omega(v)\sum_{n=0}^{N}\frac{1}{n!}\mathbf{d}^{(n)} : \mathcal{H}^{(n)}(\mathbf{v})\right)\\ &= \frac{1}{\sqrt{RT}}\mathbf{F}\cdot\sum_{n=0}^{N}\frac{1}{n!}\mathbf{d}^{(n)}\nabla_v\left(\omega(v)\mathcal{H}^{(n)}(\mathbf{v})\right)\\ &= -\frac{1}{\sqrt{RT}}\omega(v)\sum_{n=0}^{N}\frac{1}{n!}\mathbf{F}\mathbf{d}^{(n)} : \mathcal{H}^{(n+1)}(\mathbf{v}).\end{aligned} \tag{28}$$

Substituting the moments and Hermite polynomials with further simplifications, we get

$$\mathbf{F}\cdot\nabla_{\xi} f \approx -\frac{1}{\sqrt{RT}}f^{(0)}\left(\mathbf{F}\cdot\mathbf{v} - \frac{\mathbf{F}\boldsymbol{\zeta}}{2p_0} : \mathcal{H}^{(3)}(\mathbf{v}) + \frac{\mathbf{F}Q}{6p_0\sqrt{RT}} : \mathcal{H}^{(4)}(\mathbf{v}) + \cdots\right). \tag{29}$$

The second and third terms can be expanded as

$$\mathbf{F}\boldsymbol{\zeta} : \mathcal{H}^{(3)}(\mathbf{v}) = (F_k v_k v_i - 2F_i)\zeta_{ij}v_j, \tag{30a}$$

$$\mathbf{F}\mathbf{Q} : \mathcal{H}^{(4)}(\mathbf{v}) = (F_k v_k v_i + 3F_i)Q_{ijl}v_j v_l + 6F_i v_i q_k v_k - 6F_k q_k. \tag{30b}$$

The forcing term is approximated as the product of the equilibrium distribution function $f^{(0)}$ and a finite-order polynomial of $\mathbf{v}$. The leading term in parentheses corresponds to the equilibrium contribution when the distribution function is approximated by $f^{(0)}$. The subsequent terms are the higher-order moments of the non-equilibrium distribution function, notably including the stress tensor and heat flux. This hierarchical construction ensures that the approximation captures the influence of force on not only the conserved quantities (mass, momentum, energy) but also the higher-order moments of the non-equilibrium distribution function. Crucially, the formulation exhibits asymptotic consistency: as the Knudsen number $Kn \to 0$, non-equilibrium contributions diminish and it naturally recovers the equilibrium approximation.

The Hermite series converges when $\omega^{-1/2}f$ satisfies the square-integrability condition $\int \omega^{-1}|f|^2 d\xi < \infty$, where the weighting function $\omega^{1/2} \equiv (2\pi)^{-3/4}\exp\left(-|\xi - u|^2/(4RT)\right)$ corresponds to a thermodynamic equilibrium state at $2T$ [34]. This imposes the necessary asymptotic condition

$$\lim_{|\xi|\to\infty} f(\xi)\exp\left(\frac{|\xi - u|^2}{4RT}\right) = 0, \tag{31}$$

requiring f to decay faster than the equilibrium distribution at infinity. While the mean temperature T can generally satisfy Grad's 13-moment approximation as the reference temperature, the extreme thermal gradients, e.g., across shock waves, necessitate careful selection of the reference temperature. Convergence under strong temperature gradients requires that the reference temperature T_0 satisfies $T_0 \geq \frac{1}{2}T_{\max}^{\text{local}}$, where $T_{\max}^{\text{local}}$ denotes the maximum temperature within the computational domain, as validated in the shock wave simulations [45,46].

The above approximation of the forcing term is generic and applicable to a range of numerical methods, e.g., discretized velocity method, discretized unified gas kinetic scheme, and unified gas kinetic scheme. However, the neat tensor denotation is not easy to be implemented especially for the high order terms. In addition, all the Hermite polynomials and the corresponding moments are

symmetric. For three dimensional simulations, the N_{th} order symmetric tensor has N^3 components, where the number of independent components is only $(N+1)(N+2)/2$. Therefore, we re-format the above formula as follows to ease implementation.

For the weight function, we have

$$\omega(v) = \frac{1}{\sqrt{2\pi}^3}\exp\left[-\frac{(v_x+v_y+v_z)^2}{2}\right] = \omega_x\omega_y\omega_z, \tag{32}$$

where $\omega_x \equiv \frac{1}{\sqrt{2\pi}}\exp\left(-\frac{v_x^2}{2}\right)$, $\omega_y \equiv \frac{1}{\sqrt{2\pi}}\exp\left(-\frac{v_y^2}{2}\right)$, $\omega_z \equiv \frac{1}{\sqrt{2\pi}}\exp\left(-\frac{v_z^2}{2}\right)$. Consequently, by definition of n_{th} order Hermite polynomials, we have

$$\begin{aligned}
\mathcal{H}^{(n)}(v_x,v_y,v_z) &= \frac{(-1)^n}{\omega(v)}\nabla^{(n)}\omega(v)\\
&= \frac{(-1)^n}{\omega(v)}\left(\partial_x\mathbf{i}+\partial_y\mathbf{j}+\partial_z\mathbf{k}\right)^n\omega_x\omega_y\omega_z\\
&= \frac{(-1)^n}{\omega(v)}\sum_{r=0}^{n}\sum_{s=0}^{n-r}C_n^rC_{n-r}^s\partial_x^{(r)}\partial_y^{(s)}\partial_z^{(t)}\omega_x\omega_y\omega_z\mathbf{i}^r\mathbf{j}^s\mathbf{k}^t\\
&= \sum_{r=0}^{n}\sum_{s=0}^{n-r}\frac{n!}{r!s!t!}h_x^{(r)}h_y^{(s)}h_z^{(t)}\mathbf{i}^r\mathbf{j}^s\mathbf{k}^t,
\end{aligned} \tag{33}$$

where $t=n-r-s$, $h_x^{(n)} = \frac{(-1)^n}{\omega_x}\frac{d^n\omega_x}{dv_x^n}$, $h_y^{(n)} = \frac{(-1)^n}{\omega_y}\frac{d^n\omega_y}{dv_y^n}$, $h_z^{(n)} = \frac{(-1)^n}{\omega_z}\frac{d^n\omega_z}{dv_z^n}$, and $\mathbf{i},\mathbf{j},\mathbf{k}$ are the unit coordinate vector of the velocity space (v_x,v_y,v_z). Substitute Eq. (33) into Eq. (22), we have

$$\mathbf{d}^{(n)} : \mathcal{H}^{(n)}(\mathbf{v}) = \sum_{r=0}^{n}\sum_{s=0}^{n-r}C_n^rC_{n-r}^sh_x^{(r)}h_y^{(s)}h_z^{(t)}d_{x^ry^sz^t}^{(n)}, \quad \text{with,} \quad d_{x^ry^sz^t}^{(n)} = \int f h_x^{(r)}h_y^{(s)}h_z^{(t)}dv_xdv_ydv_z. \tag{34}$$

The $d_{x^ry^sz^t}^{(n)}$ are the independent variables of $\mathbf{d}^{(n)}$. Consequently, the new formula avoids repeated computations. The expansion of distribution function is rewritten as

$$f \approx f^N = \omega_x\omega_y\omega_z\sum_{n=0}^{N}\sum_{r=0}^{n}\sum_{s=0}^{n-r}\frac{1}{r!s!t!}h_x^{(r)}h_y^{(s)}h_z^{(t)}d_{x^ry^sz^t}^{(n)}. \tag{35}$$

Substituting Eq. (35) into calculation of the forcing term, and noticing

$$\frac{d}{dx}\left(h_x^{(n)}\omega_x\right) = (-1)^n\frac{d^{n+1}\omega_x}{dv_x^n} = -\omega_xh_x^{(n+1)}, \tag{36}$$

we have

$$\begin{aligned}
\mathbf{F}\cdot\nabla_\xi f^N =& \left(F_x\partial_{\xi_x}+F_y\partial_{\xi_y}+F_z\partial_{\xi_z}\right)\omega_x\omega_y\omega_z\sum_{n=0}^{N}\frac{1}{n!}\sum_{r=0}^{n}\sum_{s=0}^{n-r}\frac{n!}{r!s!t!}h_x^{(r)}h_y^{(s)}h_z^{(t)}d_{x^ry^sz^t}^{(n)}\\
=& \frac{1}{\sqrt{RT}}\omega_y\omega_z\sum_{n=0}^{N}\sum_{r=0}^{n}\sum_{s=0}^{n-r}\frac{1}{r!s!t!}\left(F_x\partial_{v_x}\omega_xh_x^{(r)}\right)h_y^{(s)}h_z^{(t)}d_{x^ry^sz^t}^{(n)}+\\
&\frac{1}{\sqrt{RT}}\omega_x\omega_z\sum_{n=0}^{N}\sum_{r=0}^{n}\sum_{s=0}^{n-r}\frac{1}{r!s!t!}\left(F_y\partial_{v_y}\omega_yh_y^{(s)}\right)h_x^{(r)}h_z^{(t)}d_{x^ry^sz^t}^{(n)}+\\
&\frac{1}{\sqrt{RT}}\omega_x\omega_y\sum_{n=0}^{N}\sum_{r=0}^{n}\sum_{s=0}^{n-r}\frac{1}{r!s!t!}\left(F_z\partial_{v_z}\omega_zh_z^{(t)}\right)h_x^{(r)}h_y^{(s)}d_{x^ry^sz^t}^{(n)}\\
=& -\frac{1}{\sqrt{RT}}\omega(v)\sum_{n=0}^{N}\sum_{r=0}^{n}\sum_{s=0}^{n-r}\frac{1}{r!s!t!}\left(F_xh_x^{(r+1)}h_y^{(s)}h_z^{(t)}+F_yh_x^{(r)}h_y^{(s+1)}h_z^{(t)}+F_zh_x^{(r)}h_y^{(s)}h_z^{(t+1)}\right)d_{x^ry^sz^t}^{(n)},
\end{aligned} \tag{37}$$

where $t=n-r-s$. This equivalent formula is easy to be implemented for any high order expansion and the independent components are only calculated once.

The two-dimensional version can be derived similarly. The final formula of the forcing term in two-dimensional case is

$$\mathbf{F}\cdot\nabla_\xi f^N = -\frac{1}{\sqrt{RT}}\omega_x\omega_y\sum_{n=0}^{N}\sum_{r=0}^{n}\frac{1}{r!(n-r)!}\left(F_xh_x^{(r+1)}h_y^{(n-r)}+F_yh_x^{(r)}h_y^{(n-r+1)}\right)d_{x^ry^{(n-r)}}^{(n)}, \tag{38}$$

where $d_{x^ry^{(n-r)}}^{(n)} = \int f h_x^{(r)}h_y^{(n-r)}dv_xdv_y$. And the one-dimensional version is

$$\mathbf{F}\cdot\nabla_\xi f^N = -\frac{1}{\sqrt{RT}}\omega_x\sum_{n=0}^{N}\frac{1}{n!}F_xh_x^{(n+1)}d^{(n)}, \tag{39}$$

where $d^{(n)} = \int f h_x^{(n)}dv_x$.

4. Shifted Gaussian-Hermite quadrature

In this work, the equation for $f(\mathbf{x}, \boldsymbol{\xi}, t)$ is solved using a discrete velocity method, where the first step is the discretization of the velocity space. Since the computational cost of DVM is primarily determined by the number of discrete velocities, for the typically low-speed transport of dense fluids, the Gaussian-Hermite quadrature can be employed to reduce the velocity-space resolution thereby the overall cost. The standard Gauss-Hermite quadrature achieves exact integration for the Maxwellian-weighted moments, i.e.,

$$\int_{-\infty}^{\infty} e^{-\xi^2} p(\xi)\,\mathrm{d}\xi \;\approx\; \sum_{i=1}^{N_\xi} w_i\, p(\xi_i), \tag{40}$$

where $\{\xi_i\}_{i=1}^{N_\xi}$ are the real roots of the Hermite polynomial $H^{(N_\xi)}(\xi)$ and the weights are given by

$$w_i = \frac{2^{N_\xi-1} N_\xi! \sqrt{\pi}}{N_\xi^2 \left[H^{(N_\xi-1)}(\xi_i)\right]^2} \tag{41}$$

for all the polynomials of degree up to $2N_\xi - 1$.

The Hermite polynomials defined above satisfy the well-known three-term recurrence

$$H^{(0)}(\xi) = 1, \qquad H^{(1)}(\xi) = 2\xi, \qquad H^{(n+1)}(\xi) = 2\xi H^{(n)}(\xi) - 2nH^{(n-1)}(\xi), \quad n \geq 1, \tag{42}$$

which is exploited to locate the quadrature nodes $\{\xi_i\}$ by finding the roots of $H^{(N_\xi)}(\xi)$ and to evaluate $H^{(N_\xi-1)}(\xi_i)$. We emphasize that these Hermite polynomials $H^{(n)}$ in Eqs. (42) – orthogonal with respect to the weight $\omega(\xi) = e^{-\xi^2}$ – differ only by a simple scaling from the Hermite polynomials $\mathcal{H}^{(n)}$ used in Eqs. (24, 25), which satisfy orthogonality with $\omega(\xi) = e^{-\xi^2/2}$. Indeed, the two sets are exactly equivalent under the linear transformation $\xi \longmapsto \xi/\sqrt{2}$ $\left(\text{or } \xi \mapsto \sqrt{2}\,\xi\right)$, yielding the explicit relation:

$$H^{(n)}(\xi) = 2^{n/2} \mathcal{H}^{(n)}\left(\xi/\sqrt{2}\right). \tag{43}$$

For an un-weighted integral $\int_{-\infty}^{\infty} p(\xi)\,\mathrm{d}\xi$, one may set $f(\xi) = e^{-\xi^2} g(\xi)$ to obtain

$$\int_{-\infty}^{\infty} f(\xi)\,\mathrm{d}\xi \;\approx\; \sum_{i=1}^{N_\xi} w_i\, g(\xi_i) \;=\; \sum_{i=1}^{N_\xi} W_i\, f(\xi_i), \quad W_i = w_i\, e^{\xi_i^2}, \tag{44}$$

which absorbs the Gaussian weights into the modified weights W_i. When the dimensionless reference velocity $\bar{u} \neq 0$ or temperature $\bar{\theta} \neq 1$, accuracy and stability can be further improved by shifting and scaling the velocity variable by

$$\xi \;=\; \sqrt{\bar{\theta}}\,\tilde{\xi} + \bar{u}, \tag{45}$$

leading to the re-scaled rule

$$\int_{-\infty}^{\infty} f(\xi)\,\mathrm{d}\xi \;\approx\; \sqrt{\bar{\theta}} \sum_{i=1}^{N_\xi} W_i\, f\left(\sqrt{\bar{\theta}}\,\tilde{\xi}_i + \bar{u}\right), \tag{46}$$

which has been shown to require fewer nodes and enhance numerical robustness in non-equilibrium flow simulations.

In wall-bounded problems, the velocity domain is $[0, \infty)$, so the half-space Gauss-Hermite quadrature is more efficient, i.e.,

$$\int_{0}^{\infty} e^{-\xi^2} p(\xi)\,\mathrm{d}\xi \;\approx\; \sum_{i=1}^{N_\xi} w_i^h\, p(\xi_i), \tag{47}$$

where $\{\xi_i\}$ are the roots of half-ranged Hermite polynomials orthogonal on $[0, \infty)$ which can be obtained by standard Gram-Schmidt orthogonalization, and the weights can be determined by

$$w_i^h = \int_0^{+\infty} \ell_i(\xi) e^{-\xi^2} d\xi \quad \text{with the Lagrange basis function} \quad \ell_i(\xi) = \prod_{\substack{j=1 \\ j\neq i}}^{N_\xi} \frac{\xi - \xi_j}{\xi_i - \xi_j}, \tag{48}$$

ensuring the exactness of the quadrature rule for polynomials up to degree $2N_\xi - 1$ [47,48]. A shift-scale transform analogous to Eq. (46) may be applied to improve stability near walls.

For d-dimensional velocity integrals, one assembles tensor-product rules as

$$\boldsymbol{\xi}_{\mathbf{i}} = (\xi_{i_1}, \ldots, \xi_{i_d}), \quad W_{\mathbf{i}} = \prod_{k=1}^{d} W_{i_k}^{(k)}. \tag{49}$$

In the mixed full/half-space domains, full- or half-space weights can be chosen along each coordinate direction.

5. Non-dimensionalization

We set $\rho_0, u_0 = \sqrt{2RT_0}, l_0$ as the reference density, velocity and length for normalization, so

$$f = \rho_0/u_0^3 \tilde{f},\ \boldsymbol{\xi} = u_0\tilde{\boldsymbol{\xi}},\ \rho = \rho_0\tilde{\rho},\ \mathbf{u} = u_0\tilde{\mathbf{u}},\ T = T_0\tilde{T},\ \mathbf{F} = u_0^2/l_0\tilde{\mathbf{F}},\ \mathbf{v} = (\boldsymbol{\xi}-\mathbf{u})/\sqrt{RT} = \sqrt{2}(\tilde{\boldsymbol{\xi}}-\tilde{\mathbf{u}})/\sqrt{\tilde{T}},$$
$$d^{(n)}_{x^r y^s z^t} = \frac{\rho_0}{u_0^3}\tilde{d}^{(n)}_{x^r y^s z^t},\ \mathbf{q} = \rho_0 RT_0 u_0\tilde{\mathbf{q}},\ \boldsymbol{\zeta} = \rho_0 RT_0\tilde{\boldsymbol{\zeta}},\ \mu_s = \rho_0 u_0 l_0\tilde{\mu}_s,\ \mu_B = \rho_0 u_0 l_0\tilde{\mu}_B,\ \tau = l_0/u_0\tilde{\tau}. \tag{50}$$

And Eq. (3) becomes

$$\frac{\partial\tilde{f}}{\partial\tilde{t}} + \tilde{\boldsymbol{\xi}}\cdot\tilde{\nabla}\tilde{f} + (\tilde{\mathbf{F}}_{\text{ext}} + \tilde{\mathbf{F}}_{\text{att}})\cdot\tilde{\nabla}_{\tilde{\xi}}\tilde{f} = -\frac{\chi(\tilde{\rho})}{\tilde{\tau}}\left[\tilde{f} - \tilde{f}^{(0)}\left(1 + (1-Pr)\frac{2\tilde{\mathbf{c}}\cdot\tilde{\mathbf{q}}}{5\tilde{p}_0\tilde{T}}\left(\frac{2\tilde{c}^2}{\tilde{T}} - 5\right)\right)\right] + \tilde{J}^{(1)} + \tilde{J}^{(2)}, \tag{51}$$

with

$$\tilde{J}^{(1)} = \rho_0 b\tilde{\rho}\chi(\tilde{\rho})\tilde{f}^{(0)}\left[\tilde{\mathbf{c}}\cdot\left(\tilde{\nabla}\ln\left(\tilde{\rho}^2\chi\tilde{T}\right) + \frac{3}{5}\left(\frac{\tilde{c}^2}{\tilde{T}} - \frac{5}{2}\right)\tilde{\nabla}\ln\tilde{T}\right) + \frac{2}{5}\left(\frac{2\tilde{\mathbf{c}}^2}{\tilde{T}} : \tilde{\nabla}\tilde{\mathbf{u}} + \left(\frac{\tilde{c}^2}{\tilde{T}} - \frac{5}{2}\right)\tilde{\nabla}\cdot\tilde{\mathbf{u}}\right)\right], \tag{52a}$$

$$\tilde{J}^{(2)} = 2\tilde{\nabla}\cdot\left(\tilde{f}^{(0)}\frac{\tilde{\mu}_B}{\tilde{p}_0}\tilde{\nabla}\cdot\tilde{\mathbf{u}}\left(\frac{\tilde{c}^2}{\tilde{T}} - \frac{3}{2}\right)\tilde{\mathbf{c}}\right). \tag{52b}$$

The forcing term is normalized as

$$\frac{u_0^2 l_0}{\rho_0}\mathbf{F}\cdot\nabla_\xi f^N = \tilde{\mathbf{F}}\cdot\nabla_{\tilde{\xi}}\tilde{f}^N$$
$$= -\sqrt{\frac{2}{\tilde{T}}}\omega(\upsilon)\sum_{n=0}^{N}\sum_{r=0}^{n}\sum_{s=0}^{n-r}\frac{1}{r!s!t!}\left(\tilde{F}_x h_x^{(r+1)}h_y^{(s)}h_z^{(t)} + \tilde{F}_y h_x^{(r)}h_y^{(s+1)}h_z^{(t)} + \tilde{F}_z h_x^{(r)}h_y^{(s)}h_z^{(t+1)}\right)\tilde{d}^{(n)}_{x^r y^s z^t}, \tag{53}$$

where

$$\tilde{d}^{(n)}_{x^r y^s z^t} = \left(\frac{2}{T}\right)^{3/2}\int \tilde{f}h_x^{(r)}h_y^{(s)}h_z^{(t)}d\tilde{\xi}_x d\tilde{\xi}_y d\tilde{\xi}_z, \tag{54}$$

which is evaluated numerically using the quadrature rule introduced in Section 4, yielding

$$\tilde{d}^{(n)}_{x^r y^s z^t} = \left(\frac{2}{T}\right)^{3/2}\sum_{i=1}^{N_{\xi_x}}\sum_{j=1}^{N_{\xi_y}}\sum_{k=1}^{N_{\xi_z}} W_i W_j W_k \tilde{f}(\tilde{\xi}_i,\tilde{\xi}_j,\tilde{\xi}_k)h_x^{(r)}(\tilde{\xi}_i)h_y^{(s)}(\tilde{\xi}_j)h_z^{(t)}(\tilde{\xi}_k). \tag{55}$$

According to the kinetic theory, the Knudsen number Kn for dense fluids is defined as

$$Kn = \frac{1}{\sqrt{2}\pi\sigma^2 n\chi(n)l_0}, \tag{56}$$

where $n = \rho/m$ is number density normalized as $\tilde{n} = n/n_0 = \tilde{\rho}$, and $\chi(n)$ describes increased collision frequency due to the dense fluid effect. By introducing the reduced number density $\eta \equiv \frac{\pi}{6}\sigma^3 n = \frac{1}{4}\rho b = \frac{1}{4}\rho_0 b\tilde{\rho}$ with $\rho_0 b = 4\eta_0$, and confinement ratio $\mathcal{R} = \frac{l_0}{\sigma}$, Kn can be reformulated as

$$Kn = \frac{1}{\sqrt{2}}\frac{1}{6\eta_0\chi(\eta_0)}\frac{1}{\mathcal{R}}\frac{1}{\tilde{\rho}}\frac{\chi(\eta_0)}{\chi(\eta)} = \frac{1}{\tilde{\rho}}\frac{\chi(\eta_0)}{\chi(\eta)}Kn^{\text{ref}},\quad \text{with}\quad Kn^{\text{ref}} = \frac{1}{\sqrt{2}}\frac{1}{6\eta_0\chi(\eta_0)}\frac{1}{\mathcal{R}}. \tag{57}$$

Therefore, the local Knudsen number Kn varies with density when the reference Knudsen number Kn^{ref} is fixed [49]. At a gas-liquid interface, the steep density gradient leads to the significant variation of Kn across the interface.

The shear and bulk viscosities are normalized as

$$\tilde{\mu}_s = \frac{5}{16}\chi(n_0)Kn^{\text{ref}}\frac{\sqrt{\pi\tilde{T}}}{\chi(\rho)}\left[\left(1 + \frac{8}{5}\eta_0\tilde{\rho}\chi(\tilde{\rho})\right)^2 + (4\eta_0\chi(\tilde{\rho})\rho)^2\right],\quad \text{and,}\quad \tilde{\mu}_B = \frac{5}{16}\sqrt{\pi\tilde{T}}\chi(n_0)Kn^{\text{ref}}\chi(\tilde{\rho})(4\eta_0\rho)^2. \tag{58}$$

The non-dimensional relaxation time becomes

$$\tilde{\tau} = \frac{2\tilde{\mu}_s}{\tilde{\rho}\tilde{T}}\frac{1}{\left(1 + \frac{8}{5}\eta_0\chi(\tilde{\rho})\tilde{\rho}\right)}. \tag{59}$$

Consequently, the dense fluid flow is also characterized by the reduced density number η_0 and the confinement ratio $\mathcal{R}$. For the sake of brevity, the tilde will be omitted from dimensionless quantities hereafter.

6. Numerical simulations

To evaluate the computational accuracy and efficiency of the proposed model for the forcing term, surface-confined flows, phase transitions and evaporation flows are studied. These simulations provide rigorous analysis for the proposed method for computing the complex non-equilibrium phenomena of dense fluids. To improve computational efficiency, the reduced distribution functions are employed for one- and two-dimensional configurations, as presented in [20].

6.1. Surface-confined flows

Surface-confinement effects cannot be ignored when the characteristic size of the flow, such as the channel width and adsorption layer, is comparable to the fluid molecular diameter. In such flows, the interactions between fluid and surface molecules play a dominant role in determining the flow behavior. Surface-confined flows exhibit significant density oscillations in the vicinity of solid surface. These oscillations are caused by spatial variation in molecular interactions near the surface and are indicative of the breakdown of the continuum hypothesis. Additionally, the molecular slip velocity and temperature jump at the surface further highlight the non-equilibrium nature of the flows. Accurate modeling of these phenomena is essential for understanding and prediction of dense fluid behavior in the confined geometries. To validate the proposed numerical model and provide a comprehensive model analysis for capturing non-equilibrium effects , we consider three representative surface-confined flows, i.e., Fourier flow, Couette flow, and Poiseuille Flow.

It should be noted that, to mitigate the computational difficulties associated with density inhomogeneity of surface-confined dense fluids, we follow [18] to use a locally-averaged density to replace the density in Eqs. (9)(10), i.e.,

$$\bar{n}(\mathbf{x}) = \frac{3}{4\pi\sigma^3}\int_{|\mathbf{r}|<\sigma} n(\mathbf{x}+\mathbf{r})d\mathbf{r}, \text{ with } \chi(n) \approx \bar{\chi}(\bar{n}). \tag{60}$$

Therefore, the gradient of density and the radial distribution function also become

$$\nabla\bar{n} \approx \frac{120}{\pi\sigma^5}\int_{|\mathbf{r}|<\sigma/2} \mathbf{r}\bar{n}(\mathbf{x}+\mathbf{r})d\mathbf{r}, \text{ with } \nabla\bar{\chi} \approx \frac{120}{\pi\sigma^5}\int_{|\mathbf{r}|<\sigma/2} \mathbf{r}\bar{\chi}(\mathbf{x}+\mathbf{r})d\mathbf{r}. \tag{61}$$

Furthermore, the relaxation time τ, Prandtl number Pr, and bulk viscosity μ_B are evaluated with the locally-averaged density. While the intermolecular interactions between surface and fluid molecules are a determining factor for the surface-confined flows, it is still a research challenge to properly consider the complex fluid/surface interactions [8]. To test and analyze the proposed numerical model for the forcing term in the kinetic equation, we simply use the Maxwellian diffuse boundary condition for the following surface-confined flows. To account for the non-equilibrium effects induced by the solid boundaries, the half-ranged Gaussian-Hermite (HGH) quadrature [47] is employed. The total number of HGH discrete velocities is $N_\xi \approx 2N+2$, where N is the Hermite expansion order. The steady-state solutions are obtained by a semi-implicit iteration scheme [17,18].

The accuracy of the computed results is assessed by comparing them with the high-resolution reference solutions obtained using uniform discrete velocities. The physical domain is resolved with a grid resolution of $\sigma = 100\delta x$, where δx is the grid spacing. The integral domain of the Vlasov force is truncated to $[-5\sigma, 5\sigma]$. The velocity space is uniformly-discretized along ξ_x and ξ_y using 150 discrete velocity points, with the domain truncated to $[-5u_0, 5u_0]$ in each direction. For the velocity-space integrals, second-order trapezoidal integration is employed. To approximate the velocity-space gradients $\nabla_\xi f$, a 4th order central difference scheme is used. This high-resolution finite-difference (FD) solution serves as the benchmark reference to evaluate the proposed model.

6.1.1. Fourier flow

Consider a steady, two-dimensional Fourier flow confined between two infinite stationary horizontal plates at different temperatures, i.e., T^{bot} at the bottom plate and T^{top} at the top plate. The simulations are conducted for $\eta_0 = 0.1, \mathcal{R} = 10, Kn^{\text{ref}} \approx 0.09$; $\eta_0 = 0.2, \mathcal{R} = 10, Kn^{\text{ref}} \approx 0.032$; and $\eta_0 = 0.2, \mathcal{R} = 20, Kn^{\text{ref}} \approx 0.016$. Additionally, three distinct temperatures, i.e., $T^{\text{top}} = 1.1$, 1.3, and 1.5 are considered with $T^{\text{bot}} = 1$. The forcing term in the governing equation is approximated using the Hermite polynomials, with the expansion order increased iteratively until convergence to capture the non-equilibrium effect caused by the molecular interaction $\mathbf{F}_{\text{att}}$. To improve computational efficiency, the classical Gaussian-Hermite quadrature is shifted, with the shifted quantities set to $\bar{\theta} = T^{\text{top}}$ and $\bar{u} = 0$.

Fig. 1 illustrates the density and temperature profiles for the Fourier flow, showing excellent agreement between the present method and the highly-accurate reference solutions. Due to the long-range intermolecular attractive forces, the density oscillations near the wall are attenuated. By varying the confinement ratio and reduced density, and consequently the Knudsen number, the transition from non-equilibrium to continuum flow regimes is systematically examined. As Kn^{ref} decreases with increasing η_0 and $\mathcal{R}$, the temperature jump at the boundaries diminishes, and the temperature profile evolves from highly nonlinear to nearly linear, consistent with the continuum theory.

As the Knudsen number decreases, fewer discrete velocities and lower expansion orders are required, reducing the overall degrees of freedom and memory cost. For $Kn^{\text{ref}} \approx 0.09$, the convergence is achieved with a 6th-order expansion and 14×14 discrete velocity points. For $Kn^{\text{ref}} \approx 0.032$ and $Kn^{\text{ref}} \approx 0.016$, a 4th order expansion and 10×10 discrete velocity points are sufficient. This trend highlights the multiscale nature and efficiency of the proposed Hermite expansion method in accurately capturing the flow behavior across a range of Knudsen numbers. The simulation results further indicate that, although no external force is imposed in the Fourier flow, intermolecular interactions act effectively as a body force and generates non-equilibrium effects, which necessitate a sufficiently high-order expansion of the forcing term for accurate simulations.

6.1.2. Couette flow

Consider a steady, two-dimensional Couette flow confined between two infinite, isothermal and horizontal plates moving in the opposite directions at a constant speed, with $U^{\text{bot}} = (-U_0, 0)$ for the bottom plate and $U^{\text{top}} = (U_0, 0)$ for the top plate. The simulations are conducted for three different Knudsen numbers, i.e., $\eta_0 = 0.1, \mathcal{R} = 10, Kn^{\text{ref}} = 0.09$; $\eta_0 = 0.2,\ \mathcal{R} = 10,\ Kn^{\text{ref}} = 0.032$; and $\eta_0 = 0.2,\ \mathcal{R} = 20,\ Kn^{\text{ref}} = 0.016$. Additionally, three flow velocities are simulated, i.e., $U_0 = 0.1$, 0.3, and 0.5.

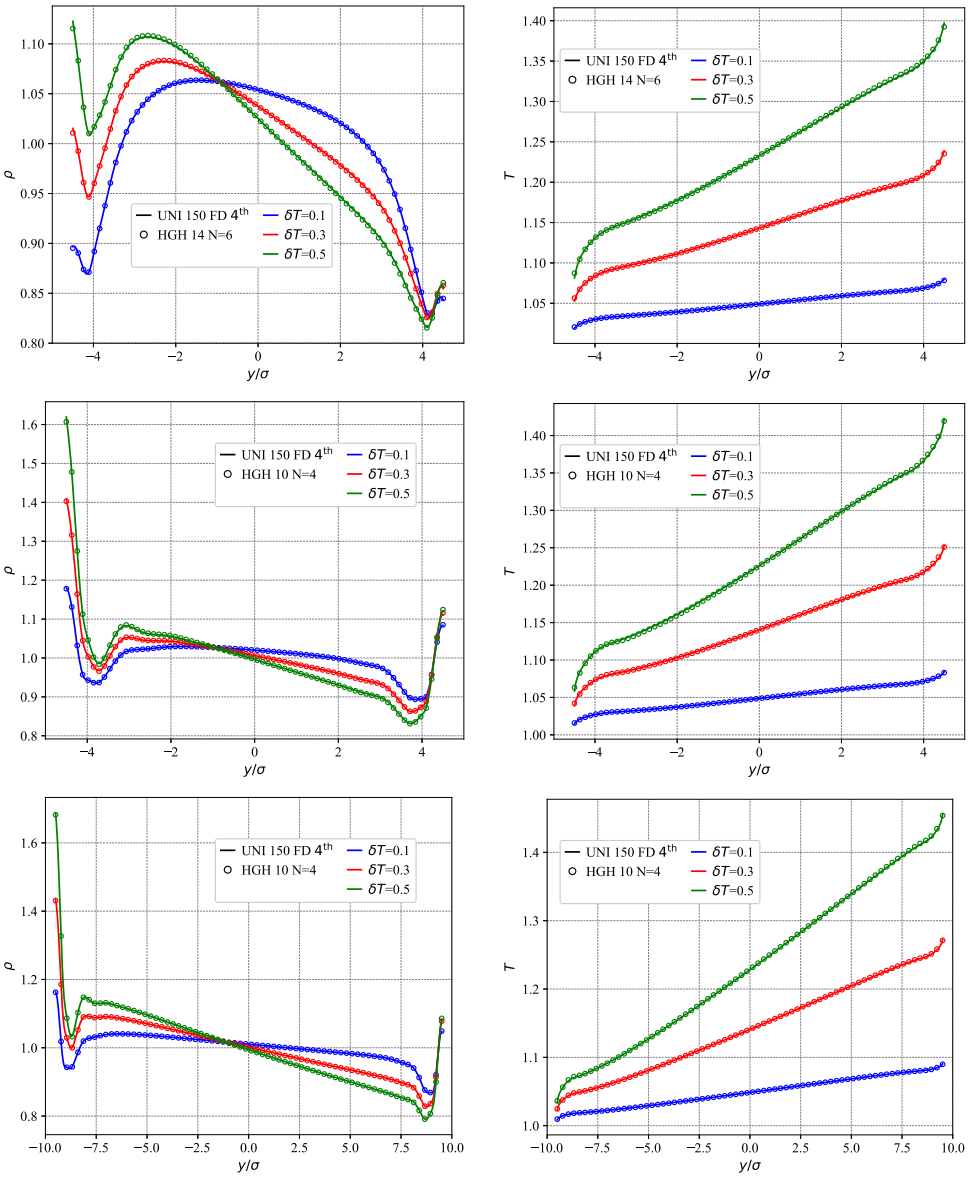

Fig. 1. The density (first column) and temperature (second column) profiles of Fourier flows. The results in the first, second, and third rows correspond to $\eta_0 = 0.1,\ \mathcal{R} = 10,\ Kn^{\mathrm{ref}} \approx 0.09$; $\eta_0 = 0.2,\ \mathcal{R} = 10,\ Kn^{\mathrm{ref}} \approx 0.032$; and $\eta_0 = 0.2,\ \mathcal{R} = 20,\ Kn^{\mathrm{ref}} \approx 0.016$, respectively. The solid lines denote the results obtained using the uniform velocity-space discretization with 150 discrete velocities and the 4th central difference scheme for $\nabla_\xi f$, while the circles indicate the results using the half-range Gaussian-Hermite quadrature. The distribution function is expanded to 6th, 4th, and 4th orders for $Kn^{\mathrm{ref}} = 0.09$, $Kn^{\mathrm{ref}} = 0.032$, and $Kn^{\mathrm{ref}} = 0.016$, respectively, with 14×14, 10×10, and 10×10 discrete velocities.

Fig. 2 presents the density, velocity, and temperature profiles of the Couette flow, which are in excellent agreement with the highly-accurate reference solutions. As the reduced density increases and the confinement ratio grows, Knudsen number becomes smaller, resulting in a reduction in slip velocity and temperature jump at the boundaries. The velocity profile evolves from non-linear to linear, and the temperature profile becomes more parabolic, similar to a continuum Couette flow.

At a fixed Knudsen number, increasing velocity of the upper plate amplifies viscous dissipation, leading to enhanced temperature in the center. The increase in temperature subsequently affects the density distribution, i.e., smaller density in the center and larger density near the plates. As Kn^{ref} decreases, the effects of viscous dissipation become more pronounced, resulting in greater variations in the temperature and density distributions.

When Kn decreases, the computational cost becomes smaller as the Hermite expansion order and the number of discrete velocities can be smaller. For $Kn^{\mathrm{ref}} \approx 0.09$ and $Kn^{\mathrm{ref}} \approx 0.032$, the distribution function converges with a 6th order expansion and 14×14 discrete velocities. For $Kn^{\mathrm{ref}} \approx 0.016$, a 4th order expansion and 10×10 discrete velocities suffice. This reduction highlights the multiscale nature and efficiency of the proposed method in accurately capturing flow physics across a wide range of Knudsen numbers.

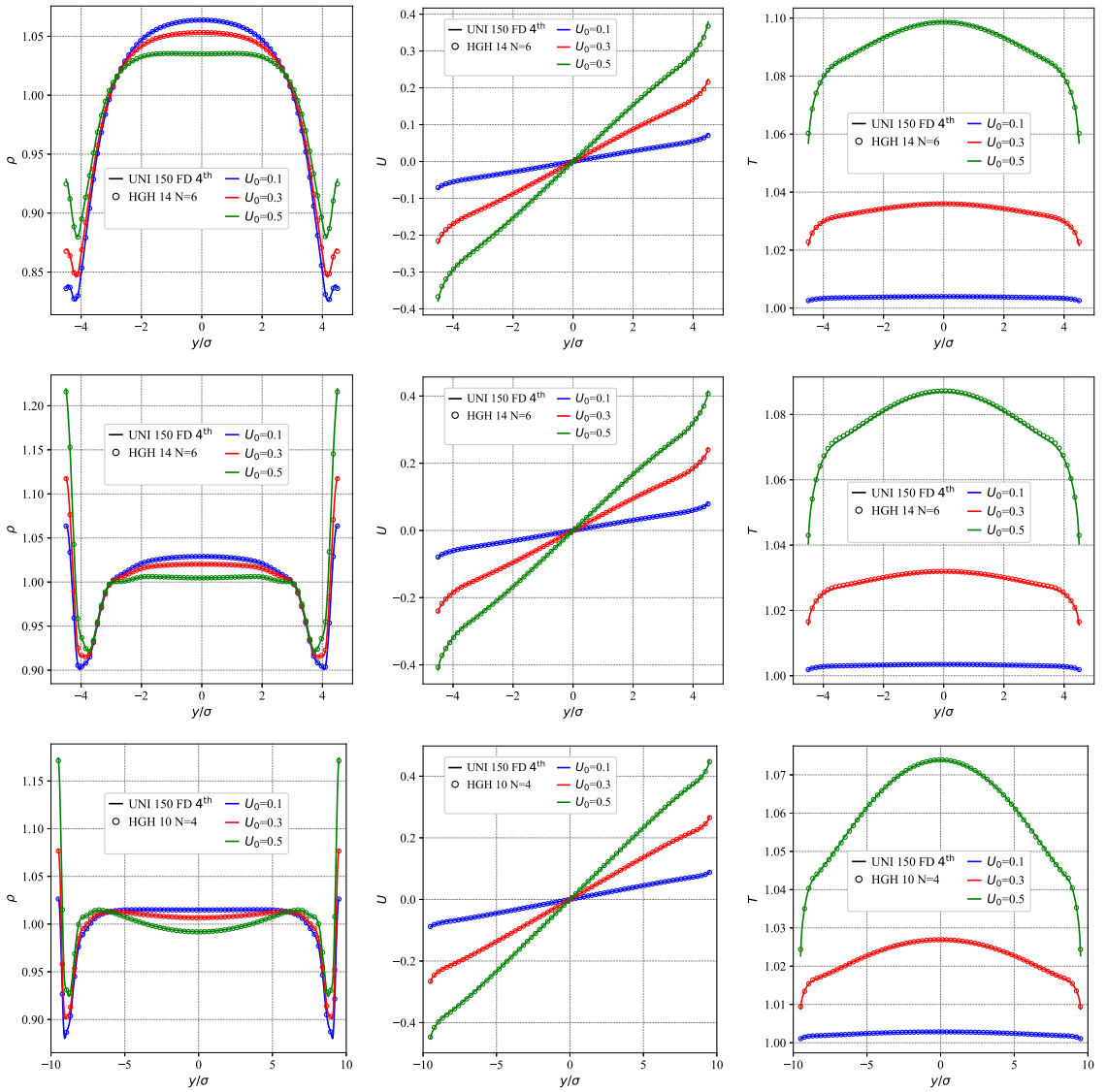

Fig. 2. The density (first column), velocity (second column), and temperature (third column) profiles of Couette flows. The results in the first, second, and third rows correspond to $\eta_0 = 0.1, \mathcal{R} = 10, Kn^{\text{ref}} \approx 0.09$; $\eta_0 = 0.2, \mathcal{R} = 10, Kn^{\text{ref}} \approx 0.032$; and $\eta_0 = 0.2,\ \mathcal{R} = 20,\ Kn^{\text{ref}} \approx 0.016$, respectively. The solid lines denote the results obtained using the uniform velocity-space discretization with 150 discrete velocities and the 4th order central difference scheme for $\nabla_\xi f$, while the circles indicate the results based on the half-range Gaussian-Hermite quadrature. The distribution function is expanded to 6th, 6th, and 4th orders for $Kn^{\text{ref}} = 0.09$, $Kn^{\text{ref}} = 0.032$, and $Kn^{\text{ref}} = 0.016$, respectively, with 14×14, 14×14, and 10×10 discrete velocities.

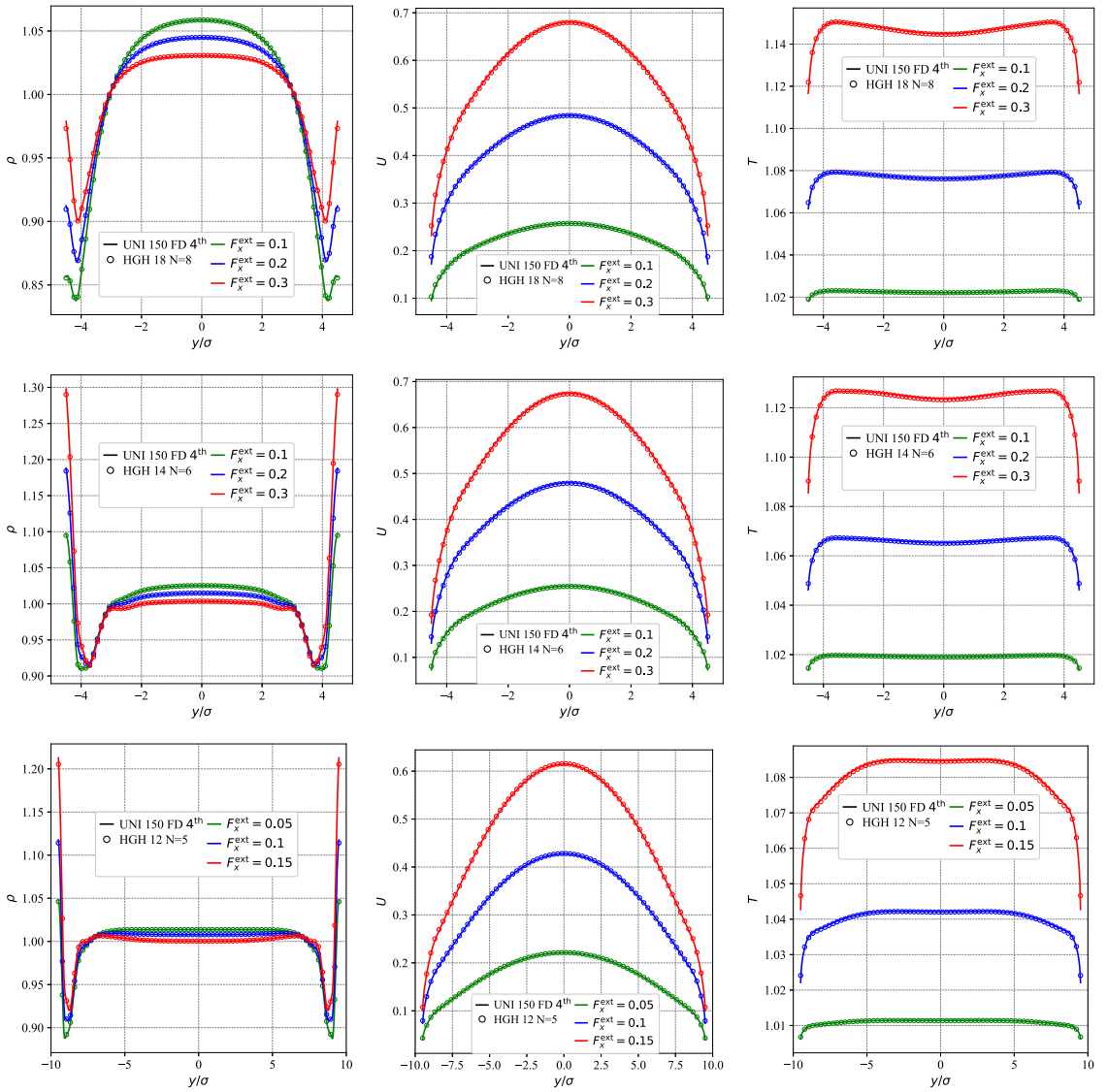

Fig. 3. The density (first column), velocity (second column), and temperature (third column) profiles of Poiseuille flow. The results in the first, second, and third rows correspond to $\eta_0 = 0.1, \mathcal{R} = 10, Kn^{\text{ref}} \approx 0.09$; $\eta_0 = 0.2, \mathcal{R} = 10, Kn^{\text{ref}} \approx 0.032$; and $\eta_0 = 0.2, \mathcal{R} = 20, Kn^{\text{ref}} \approx 0.016$, respectively. The solid lines denote the results obtained using the uniform velocity-space discretization with 150 discrete velocities and the 4th order central difference scheme for $\nabla_\xi f$, while the circles indicate the results based on the half-range Gaussian-Hermite quadrature. The distribution function is expanded to 8th, 6th, and 5th orders for $Kn^{\text{ref}} = 0.09$, $Kn^{\text{ref}} = 0.032$, and $Kn^{\text{ref}} = 0.016$, respectively, with 18×18, 14×14, and 12×12 discrete velocities.

6.1.3. Poiseuille flow

Driven by an external force $\mathbf{F}_{\text{ext}} = \left(F_x^{\text{ext}}, 0\right)$, a steady Poiseuille flow confined between two infinite, stationary and isothermal horizontal plates is simulated. In the incompressible continuum limit, the velocity profile becomes parabolic. The simulations are performed for $\eta_0 = 0.1, \mathcal{R} = 10, Kn^{\text{ref}} \approx 0.09$; $\eta_0 = 0.2, \mathcal{R} = 10, Kn^{\text{ref}} \approx 0.032$; and $\eta_0 = 0.2, \mathcal{R} = 20, Kn^{\text{ref}} \approx 0.016$, with the external force being $F_x^{\text{ext}} = 0.1, 0.2, 0.3$ for $Kn^{\text{ref}} \approx 0.09$ and 0.032, and $F_x^{\text{ext}} = 0.05, 0.1, 0.15$ for $Kn^{\text{ref}} \approx 0.016$. The forcing term in the governing equation is approximated by the Hermite polynomials. We systematically increase the Hermite expansion order to ensure convergence and to accurately capture the non-equilibrium effects of the Poiseuille flow. For the cases with large flow velocities, a shifted Gaussian-Hermite quadrature is employed to increase computational efficiency, with the shift determined by the maximum temperature, $\bar{\theta} = T^{\max}$, and the average velocity, $\bar{u} = u^{\text{ave}}$. Note, the forcing term here includes the external force $\mathbf{F}_{\text{ext}}$ and the long-range intermolecular interactions.

Fig. 3 shows the excellent agreement between the present method and the reference solutions. For large Kn^{ref}, the temperature profile exhibits a distinct double-peak profile, a hallmark of non-equilibrium Poiseuille flow. As Kn^{ref} decreases, the double-peak feature in the temperature profile diminishes and the velocity profile becomes more parabolic, with reduction in the slip velocities and temperature jumps at the walls. The viscous dissipation becomes more pronounced with increasing external force and reducing Kn^{ref}.

As Kn^{ref} decreases, lower expansion orders and fewer discrete velocities are required for convergence, i.e., for $Kn^{\text{ref}} \approx 0.09$, 8th order expansion and 18×18 discrete velocities; for $Kn^{\text{ref}} \approx 0.032$, 6th order expansion and 14×14 discrete velocities; for $Kn^{\text{ref}} \approx 0.016$, 5th order expansion and 12×12 discrete velocities. Therefore, the present method is able to efficiently and accurately capture flow physics across a wide range of Kn^{ref}.

To further evaluate the computational efficiency in comparison with the 4th order central difference method, the simulations are conducted using the uniform discrete velocities with 20, 50, 100, and 120 velocity points respectively, alongside the Gaussian-Hermite quadratures using 8, 14 and 18 discrete velocities. These configurations correspond to algebraic accuracies of 7th, 13th and 17th orders, together with the Hermite expansion orders of 3rd, 6th and 8th respectively. The results, shown in Fig. 4, highlight the superior precision of the present method, which achieves comparable accuracy with significantly fewer discrete velocities.

Table 1 compares the computational efficiency of the present method with the classical 4th order central difference scheme. The temperature error of the proposed method, defined by

$$E_T = \sqrt{\frac{\sum_j \left(T_j - T_j^{\text{ref}}\right)^2}{\sum_j \left(T_j - 1\right)^2}},$$

remains below 0.5% in all the cases. With the same time step Δt, the proposed method achieves up to one order of magnitude acceleration owing to the reduced number of discrete velocities. The speedup is smaller than the reduction of number of discrete velocities because the evaluation of high-order moments introduces additional computational cost. As the reference Knudsen number decreases, fewer discrete velocities and lower expansion orders are required for convergence, which further increases the overall acceleration. The method also exhibits enhanced numerical stability, allowing larger time steps, and requires fewer iterations to reach steady convergence. Consequently, the total computational time is reduced in comparison with the uniform discretisation, e.g., for $Kn^{\text{ref}} \approx 0.016$, the speedup is 566. These results demonstrate the substantial efficiency advantage of the proposed method over the 4th order central difference method. For the conventional DVM-type iterative solvers, the slow convergence and restrictive time-step requirement at small Knudsen numbers could be further alleviated by incorporating advanced acceleration strategies such as the General Synthetic Iterative Scheme (GSIS), which is expected to substantially reduce the iteration count and provide additional speedup [50,51].

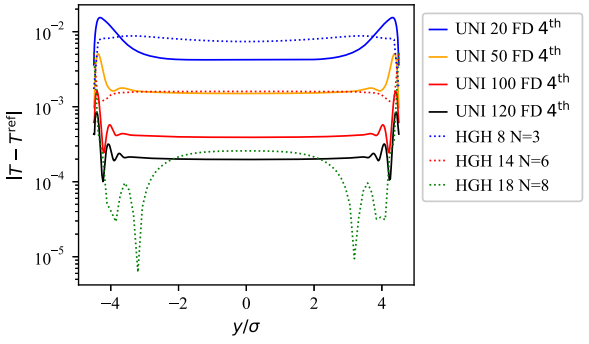

Fig. 4. In comparison with the highly-accurate reference temperature of the Poiseuille flow at $\eta_0 = 0.1$, $\mathcal{R} = 10$, $Kn^{\text{ref}} \approx 0.09$, $F_x^{\text{ext}} = 0.3$.

Table 1
Comparison of the computational time for the Poiseuille flow at $F_x^{\text{ext}} = 0.3$ and $F_x^{\text{ext}} = 0.15$.

Kn^{ref}	Method	Discrete velocities number	Discrete velocities number reduction factor	Expansion order	$\Delta t/\Delta x$	Iterative step	CPU time (s)	Speedup ratio	Temperature error (%)
0.09	Uniform	150×150	—	—	1	24104	35226.6	—	—
	HGH	18×18	64.31	8	1	24104	3451.71	10.20	0.34
					10	2231	346.06	101.79	
0.032	Uniform	150×150	—	—	1	19540	31921.46	—	—
	HGH	14×14	114.7	6	1	19540	975.76	32.71	0.28
					10	1954	97.5	327.40	
0.016	Uniform	150×150	—	—	1	55040	199342.58	—	—
	HGH	12×12	156.25	5	1	55040	3531.47	56.44	0.42
					10	5504	352.17	566.04	

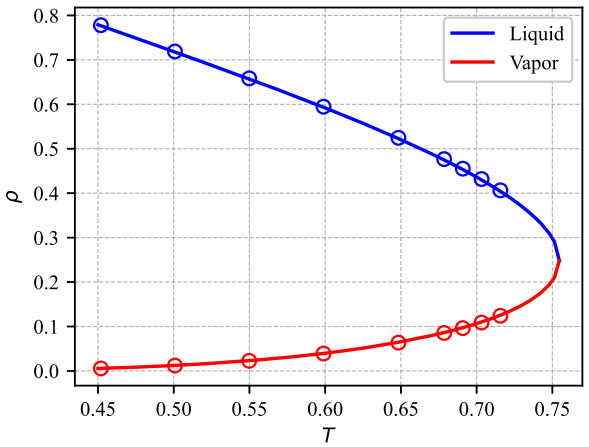

Fig. 5. Liquid-vapor coexistence curve at equilibrium: the solid lines are the numerical results of the present method while the circles are the solutions of Eq. (62).

6.2. Phase transition and interfacial dynamics

When the system temperature is below the critical temperature, a liquid-vapor interface emerges, characterized by a significant density contrast between the phases, resulting in molecular mean free paths differing by several orders of magnitude. The vapor phase adjacent to the interface, called Knudsen layer, is rarefied which cannot be described by the continuum theory. In this section, the proposed method will be validated and analyzed for liquid-vapor coexistence at equilibrium and non-equilibrium evaporative flows.

6.2.1. Liquid-vapor coexistence at equilibrium

Under a given temperature, equilibrium between the liquid and vapor phases is established when the liquid evaporates and reaches its saturation pressure. At this equilibrium state, the temperature T, pressure p, and chemical potential ϕ_c of both phases are identical [52]. The equilibrium conditions for hard sphere molecules are given by

$$T = T_g = T_l, \tag{62a}$$

$$\begin{aligned} p &= \rho_g \frac{k_B}{m} T_g \frac{(1+\eta_g+\eta_g^2-\eta_g^3)}{(1-\eta_g)^3} - \frac{4\pi\sigma^3}{3}\rho_g^2 \\ &= \rho_l \frac{k_B}{m} T_l \frac{(1+\eta_l+\eta_l^2-\eta_l^3)}{(1-\eta_l)^3} - \frac{4\pi\sigma^3}{3}\rho_l^2, \end{aligned} \tag{62b}$$

$$\begin{aligned} \phi_c &= k_B T_g \left[\eta_g \frac{8-9\eta_g+3\eta_g^2}{(1-\eta_g)^3} + \ln \eta_g \right] - 16\epsilon_p \eta_g \\ &= k_B T_l \left[\eta_l \frac{8-9\eta_l+3\eta_l^2}{(1-\eta_l)^3} + \ln \eta_l \right] - 16\epsilon_p \eta_l, \end{aligned} \tag{62c}$$

where the subscripts g and l denote the quantities associated with the vapor and liquid phases, respectively.

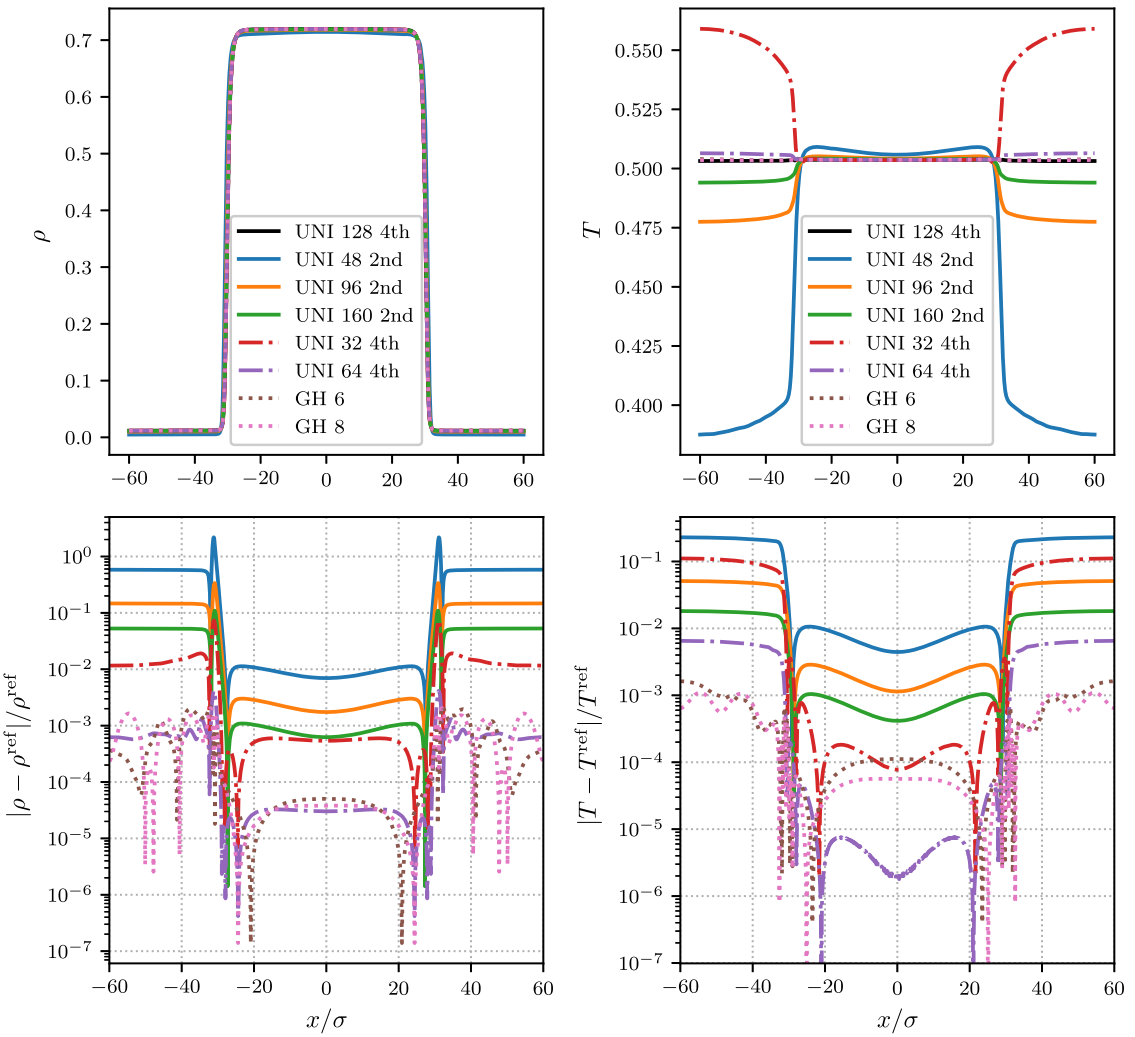

Fig. 6. The density (top left) and temperature (top right) profiles and the relative errors in density (bottom left) and temperature (bottom right) for the liquid-vapor coexistence at equilibrium.

The simulations are conducted with the reduced density parameter $\eta_0 = \rho_0 b/4 = \pi/6$, the molecular diameter of the reference length ($\sigma/l_0 = 1$), and the computational domain is $[-60\sigma, 60\sigma]$ with $\sigma = 10\delta x$, where δx is the spatial interval. The boundary condition is periodic. The Gaussian integration with eight discrete velocities is employed under equilibrium conditions ($\bar{\theta} = T^{eq}$ and $\bar{u} = 0$), while the initial density field is set as

$$\rho(x) = \rho_g + \frac{\rho_l - \rho_g}{2}[\tanh(x + 30\sigma) - \tanh(x - 30\sigma)]. \tag{63}$$

Fig. 5 shows that the computed liquid-vapor coexistence curve at equilibrium agrees well with the solution of Eq. (62).

To assess the accuracy of different discretization strategies for evaluating the velocity-space gradient $\nabla_\xi f$, we conduct a systematic comparison with a highly-accurate reference solution using the 4th order central difference scheme, which is computed with 128 uniformly distributed velocity points in the velocity interval $[-5u_0, 5u_0]$. Three approaches are tested: (1) the 2nd order central difference scheme with 48, 96, and 160 velocity points; (2) the 4th order central difference scheme with 32 and 64 velocity points; and (3) the present method with 0th order expansion and 6 or 8 Gauss-Hermite quadrature points. In all the cases, the physical space is discretized with $\sigma = 10\,\delta x$.

As illustrated in Fig. 6, the 2nd order scheme exhibits slow convergence, requiring over 160 velocity points to achieve acceptable accuracy. The 4th order scheme improves convergence, but still suffers from large errors in temperature with 32 velocity points. By contrast, the present method achieves significantly more accurate results with only 6–8 quadrature points.

6.2.2. *Non-equilibrium evaporative flow*

Here, non-equilibrium evaporative flows are considered to evaluate the proposed method. The simulation setup is illustrated in Fig. 7. The simulations are performed with the reduced density number of $\eta_0 = \rho_0 b/4 = \pi/6$, and the computational domain extends

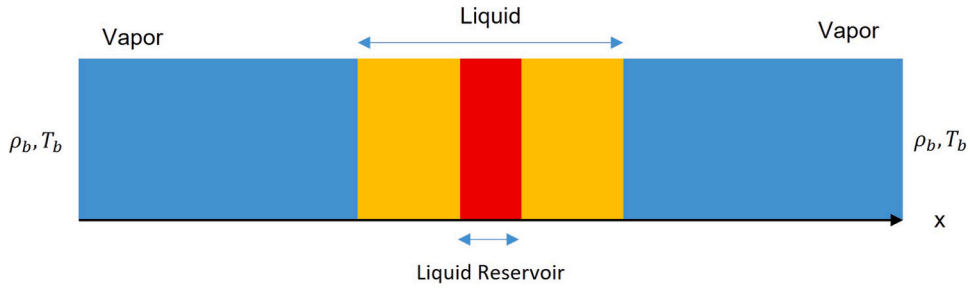

Fig. 7. The schematic diagram of one dimensional non-equilibrium evaporative flow.

from -25σ to 25σ. The reference length l_0 is set to be 50σ, with the molecular diameter of the reference length $\sigma/l_0 = 0.02$. The initial conditions are $T = 0.5$, $\rho_g = 0.012$, $\rho_l = 0.719$. The density distribution is initialized as

$$\rho(x) = \rho_g + \frac{\rho_l - \rho_g}{2}\left[\tanh\left(x + \frac{25}{2}\sigma\right) - \tanh\left(x - \frac{25}{2}\sigma\right)\right]. \tag{64}$$

In the region where $x \in (-2\sigma, 2\sigma)$, the fluid properties are held constant with $T_l = 0.5$, $\rho_l = 0.719$, and $u_l = 0$. At the boundaries, the density, temperature, and velocity are fixed at $\rho_b = \frac{1}{2}\rho_g$, $T_b = 0.25$, and $u_b = 0$, respectively. The boundary conditions for the distribution function are defined as

$$f\left(-\frac{L}{2}, \xi\right) = \frac{\rho_b}{(2\pi T_b)^{3/2}} \exp\left(-\frac{\xi^2}{2T_b}\right), \quad \xi > 0, \tag{65}$$

$$f\left(\frac{L}{2}, \xi\right) = \frac{\rho_b}{(2\pi T_b)^{3/2}} \exp\left(-\frac{\xi^2}{2T_b}\right), \quad \xi < 0. \tag{66}$$

A scaled Gaussian-Hermite quadrature ($\bar{\theta} = 0.5, \bar{u} = 0$) with eight discrete velocities is employed to discretize the velocity space, and the forcing term is expanded to 3rd order. For comparison, the gradient $\nabla_\xi f$ is also computed using a 4th order central difference scheme with 100 uniformly distributed velocity points over the interval $[-5u_0, 5u_0]$, and the results serve as the reference solution. The transient results are computed using a first-order Euler time integration scheme combined with a 2nd order finite difference scheme for convection [20]. The spatial and temporal intervals are set as $\delta x = \sigma/10$, $\delta t/\delta x \approx 9.279 \times 10^{-2}$, respectively. Fig. 8 shows the evolution of the flow field with the unity t corresponding to 5×10^4 simulation time steps. As the liquid begins to evaporate, the liquid-vapor interface shifts inward and eventually reaches a steady state. Rapid variations of the macroscopic quantities are observed near the interface. At various time steps, the results obtained with the scaled Gaussian-Hermite quadrature are in excellent agreement with those obtained by the uniformly discretized method, confirming the accuracy of the present method.

To further assess the impact of the non-equilibrium effects of the forcing term, the simulations are carried out using 0th, 2nd, 3rd, and 4th, respectively as shown in Fig. 9 (left). The 0th order expansion, corresponding to an equilibrium approximation of the distribution function, exhibits significant errors. Fig. 9 (right) shows significant variation of Kn across the interface, indicating strong non-equilibrium effect at the interface and Knudsen layer. As the expansion order increases, the higher-order moments which are essential for non-equilibrium effects can be captured well.

High-order expansions are essential in the regions with strong non-equilibrium effects, particularly in the Knudsen layer, while lower-order expansions may be sufficient in other regions. To further improve computational efficiency, we introduce an adaptive Hermite expansion strategy that dynamically adjusts the expansion order in space and time. The expansion is terminated locally once the relative change between successive approximations satisfies

$$\frac{\|f - f_N\|}{\|f\|} < \varepsilon,$$

where $\varepsilon = 10^{-3}$. This adaptive approach allows the solver to retain high-order accuracy in the strong non-equilibrium regions while avoiding unnecessary computations in near-equilibrium zones.

To verify the accuracy and efficiency of this adaptive approach, we consider a test case with a reduced vapour density at the outlets, $\rho_b = \frac{1}{5}\rho_g$, while keeping all the other parameters unchanged. The reference solution is obtained using 128 uniformly spaced velocity points and a 4th order central difference scheme for $\nabla_\xi f$. The present method employs 10 Gauss-Hermite nodes, with the expansion order determined adaptively at each point in space and time according to the above convergence criterion.

Fig. 10 presents the evolution of density, velocity, and temperature during the evaporation process. Due to the lower vapour density at the outlet, the fluid molecules evaporate from the liquid more rapidly, and the interface exhibits steep gradients in both density and temperature. The adaptive scheme provides accurate results in excellent agreement with the reference solution.

To further analyze the adaptive scheme, we extract the local expansion order and Knudsen number at $t = 4$. As shown in Fig. 11, the expansion order remains low (mostly 0th order) within the liquid, where local Knudsen numbers are small. By contrast, near the interface and in the vapor phase, the required expansion order increases notably. This is due to the enhanced non-equilibrium effects, which stem from the combination of steep gradients in macroscopic quantities across the interface and the pronounced drop in density. These results confirm that the adaptive scheme can effectively capture multiscale features of the flow, maintaining high accuracy while significantly reducing computational cost.

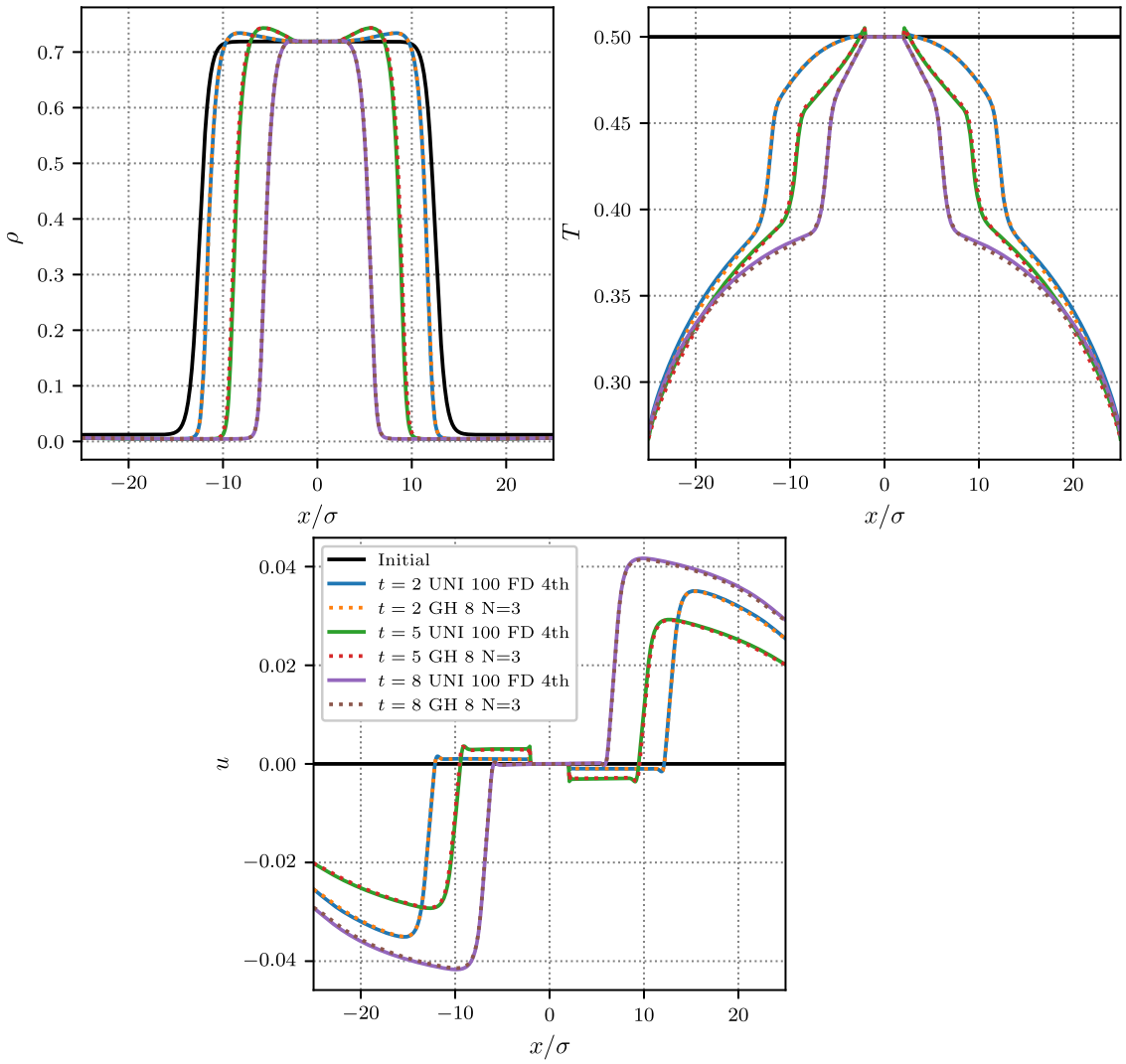

Fig. 8. Density (top left), velocity (top right) and temperature (bottom) of evaporative flow varying with time at $\rho_b = \frac{1}{2}\rho_g$. Unit time t corresponds to 5×10^4 simulation steps.

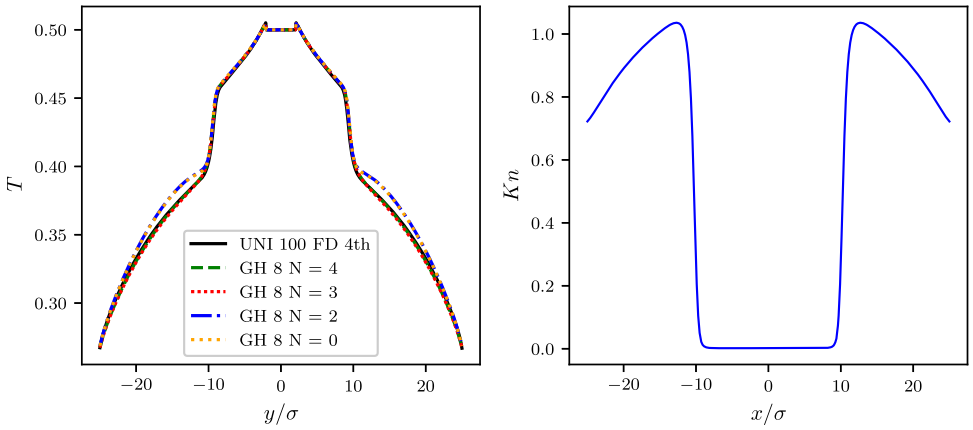

Fig. 9. Temperature (left) and *Kn* number (right) distribution of evaporative flow under various expansion order at $t = 5$.

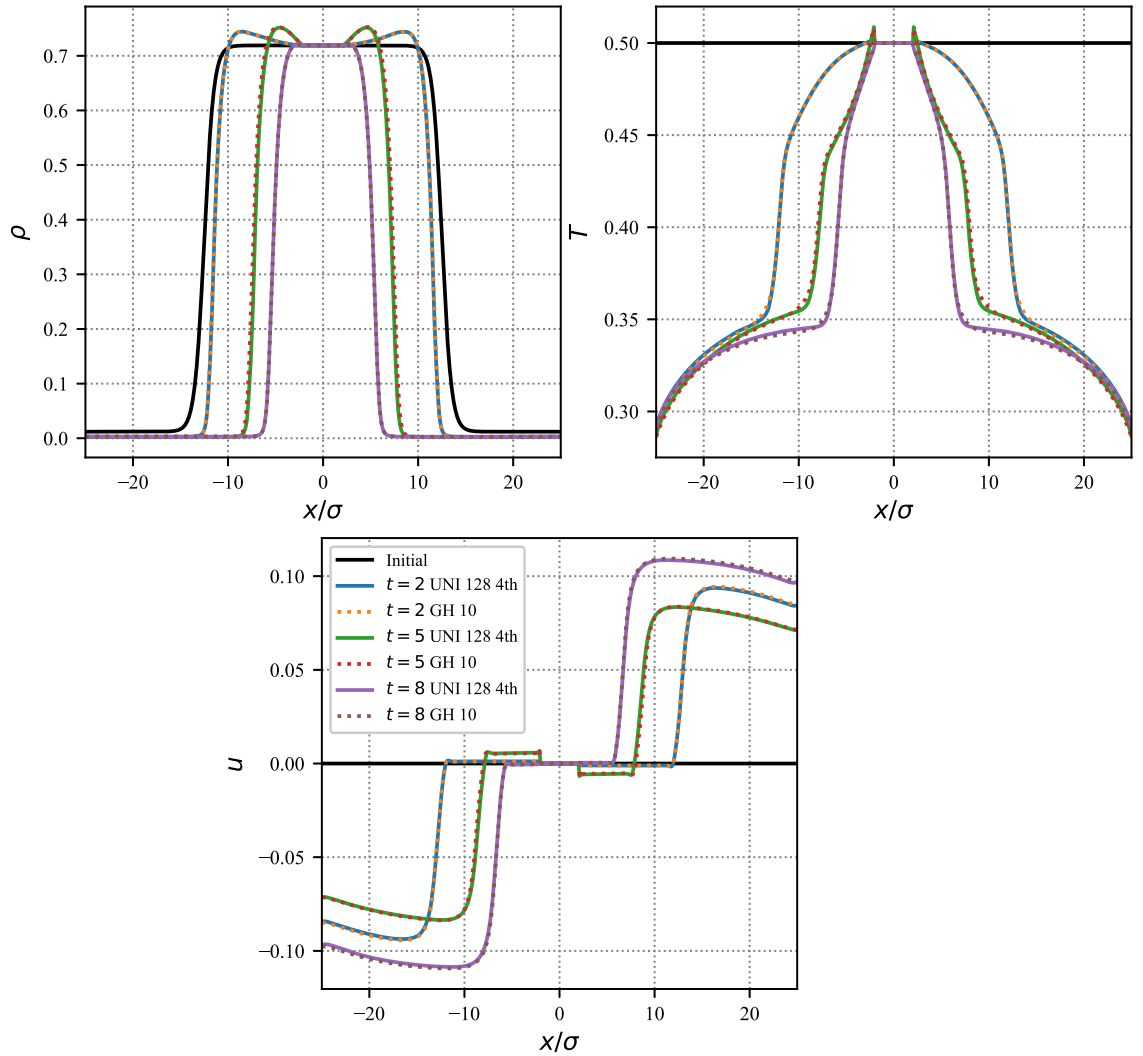

Fig. 10. Density (top left), velocity (top right) and temperature (bottom) of evaporative flow varying with time at $\rho_b = \frac{1}{5}\rho_g$. Unit time t corresponds to 5×10^4 simulation steps.

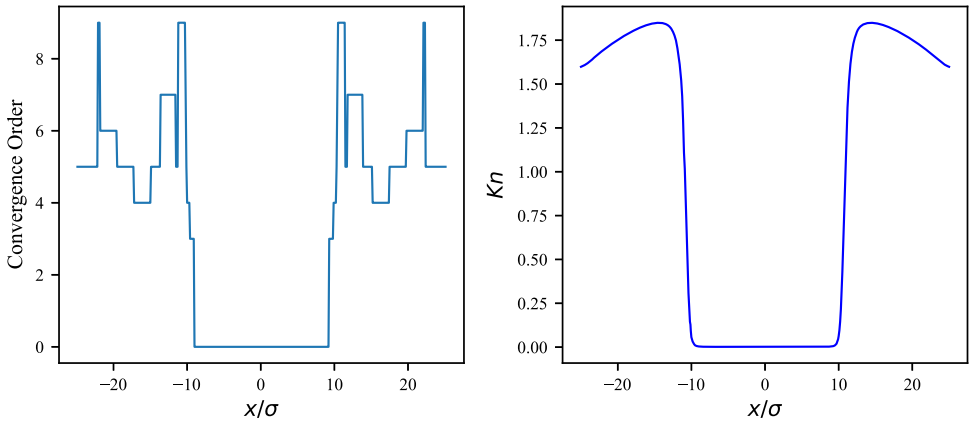

Fig. 11. Convergence order (left) and *Kn* number (right) distribution of evaporative flow under various expansion order at $t = 4$.

7. Conclusions

This work presents a novel numerical model for the forcing term to improve accuracy and efficiency of the kinetic simulations, which has been validated and analyzed for surface-confined non-equilibrium flows (Fourier, Couette, and Poiseuille flows), phase transition, and non-equilibrium evaporative flows. Compared with the conventional 4th order central difference method employing uniform velocity-space discretization, the present method, combined with the rescaled Gaussian-Hermite quadrature, requires fewer discrete velocity points and permits larger temporal intervals, thus achieving computational speedup of approximately two- to three-order of magnitude for two-dimensional cases. Therefore, the proposed model can provide an accurate and efficient computational tool to tackle phase transition, non-equilibrium evaporative flows and surface-confined flows at the micro- and nano-scales.

CRediT authorship contribution statement

Zuoxu Li: Writing – original draft, Visualization, Validation, Software, Methodology, Investigation, Formal analysis, Data curation, Conceptualization; **Shaokang Li:** Software, Methodology; **Tianbai Xiao:** Writing – review & editing, Supervision, Software, Formal analysis; **Yonghao Zhang:** Writing – review & editing, Supervision, Resources, Project administration, Methodology, Funding acquisition, Formal analysis, Conceptualization.

Data availability

Data will be made available on request.

Declaration of competing interest

The authors declare that they have no known competing financial interests or personal relationships that could have appeared to influence the work reported in this paper.

Acknowledgement

The current research is funded by the National Science Foundation of China (No. 12302381). The computing resources provided by Hefei Advanced Computing Center and ORISE Supercomputer are acknowledged.

References

[1] M.M. Nahar, B. Ma, K. Guye, Q.H. Chau, J. Padilla, M. Iyengar, D. Agonafer, Review article: microscale evaporative cooling technologies for high heat flux microelectronics devices: background and recent advances, 2021. https://doi.org/10.1016/j.applthermaleng.2021.117109
[2] M. Gallo, F. Magaletti, A. Georgoulas, M. Marengo, J.D. Coninck, C.M. Casciola, A nanoscale view of the origin of boiling and its dynamics, Nat. Commun. 14 (1) (2023) 06428. https://doi.org/10.1038/s41467-023-41959-3
[3] J. Wang, Y. Wang, B. Li, Q. Wang, S. Meng, R. Chen, H. Wu, F. Wang, Molecular understanding of phase behavior of hydrocarbon mixtures in nanopores and their influence on recovery dynamics, Theor. Appl. Mech. Lett. 15 (4) (2025) 0100589. https://doi.org/10.1016/j.taml.2025.100589
[4] S. Chatterjee, Paras, H. Hu, M. Chakraborty, A review of nano and microscale heat transfer: an experimental and molecular dynamics perspective, Processes 11 (9) (2023). https://doi.org/10.3390/pr11092769
[5] R. Meland, A. Frezzotti, T. Ytrehus, B. rn Hafskjold, Nonequilibrium molecular-dynamics simulation of net evaporation and net condensation, and evaluation of the gas-kinetic boundary condition at the interphase, Phys. Fluids 16 (2) (2004) 223–243. https://doi.org/10.1063/1.1630797
[6] L. De Sobrino, On the kinetic theory of a van der Waals gas, Can. J. Phys. 45 (2) (1967) 363–385. https://doi.org/10.1139/p67-035
[7] E.S. Benilov, M.S. Benilov, The Enskog-Vlasov equation: a kinetic model describing gas, liquid, and solid, 10, 2019, p. 103205. https://doi.org/10.1088/1742-5468/ab3ccf
[8] B. Shan, M. Torrilhon, Z. Guo, Y. Zhang, Molecular kinetic modelling of nanoscale confined flows, 2025. https://doi.org/10.1017/jfm.2025.10204
[9] H. Struchtrup, A. Frezzotti, Twenty-six moment equations for the Enskog-Vlasov equation, J. Fluid Mech. 940 (2022). https://doi.org/10.1017/jfm.2022.98
[10] M. Sadr, M.H. Gorji, A continuous stochastic model for non-equilibrium dense gases, Phys. Fluids 29 (12) (2017) 122007. https://doi.org/10.1063/1.5004409
[11] A. Frezzotti, A particle scheme for the numerical solution of the Enskog equation, PLXPAGE05 9 1329–1335. https://doi.org/10.1063/1.869247
[12] S. Busuioc, A. Frezzotti, L. Gibelli, A weighted particle scheme for Enskog-Vlasov equation to simulate spherical nano-droplets/bubbles, J. Comput. Phys. 475 (2023) 111873. https://doi.org/10.1016/j.jcp.2022.111873
[13] H. Struchtrup, H. Jahandideh, A. Couteau, A. Frezzotti, Heat transfer and evaporation processes from the Enskog-Vlasov equation and its moment equations, Int. J. Heat Mass Transf. 223 (2024) 125238. https://doi.org/10.1016/j.ijheatmasstransfer.2024.125238
[14] M. Sadr, M. Pfeiffer, M.H. Gorji, Fokker-Planck-Poisson kinetics: multi-phase flow beyond equilibrium, J. Fluid Mech. 920 (2021). https://doi.org/10.1017/jfm.2021.461
[15] L. Wu, Y. Zhang, J.M. Reese, Fast spectral solution of the generalized Enskog equation for dense gases, J. Comput. Phys. 303 (2015) 66–79. https://doi.org/10.1016/j.jcp.2015.09.034
[16] L. Wu, H. Liu, J.M. Reese, Y. Zhang, Non-equilibrium dynamics of dense gas under tight confinement, J. Fluid Mech. 794 (2016) 252–266. https://doi.org/10.1017/jfm.2016.173
[17] P. Wang, L. Wu, M.T. Ho, J. Li, Z.-H. Li, Y. Zhang, The kinetic Shakhov-Enskog model for non-equilibrium flow of dense gases, J. Fluid Mech. 883 (2020). https://doi.org/10.1017/jfm.2019.915
[18] W. Su, L. Gibelli, J. Li, M.K. Borg, Y. Zhang, Kinetic modeling of nonequilibrium flow of hard-sphere dense gases, Phys. Rev. Fluids 8 (2023) 13401. https://doi.org/10.1103/PhysRevFluids.8.013401
[19] B. Shan, W. Su, L. Gibelli, Y. Zhang, Molecular kinetic modelling of non-equilibrium transport of confined van der waals fluids, J. Fluid Mech. 976 (7) (2023). https://doi.org/10.1017/jfm.2023.893
[20] S. Li, W. Su, B. Shan, Z. Li, L. Gibelli, Y. Zhang, Molecular kinetic modelling of non-equilibrium evaporative flows, J. Fluid Mech. 994 (16). https://doi.org/10.1017/jfm.2024.605
[21] S. Li, L. Gibelli, Y. Zhang, Non-equilibrium evaporation of lennard-jones fluids: Enskog-vlasov theory and hertz-knudsen model, 2025. https://arxiv.org/abs/2508.15785.

[22] M. Tij, A. Santos, Perturbation analysis of a stationary nonequilibrium flow generated by an external force, J. Stat. Phys. 76 (5) (1994) 1399–1414. https://doi.org/10.1007/BF02187068
[23] D. Guéry-Odelin, J.G. Muga, M. á José Ruiz-Montero, E. Trizac, Nonequilibrium solutions of the boltzmann equation under the action of an external force, Phys. Rev. Lett. 112 (2014) 180602. https://doi.org/10.1103/PhysRevLett.112.180602
[24] T. Xiao, K. Xu, Q. Cai, T. Qian, An investigation of non-equilibrium heat transport in a gas system under external force field, Int. J. Heat Mass Transf. 126 (2018) 362–379. https://doi.org/10.1016/j.ijheatmasstransfer.2018.05.035
[25] S. Chen, C. Lin, D. Li, H. Lai, Burnett-level discrete boltzmann modeling of compressible flows under force, 056114, 05 2025 37. https://doi.org/10.1063/5.0269274
[26] A. Frezzotti, P. Barbante, Kinetic theory aspects of non-equilibrium liquid-vapor flows, Mech. Eng. Rev. 4 (2) (2017). https://doi.org/10.1299/mer.16-00540
[27] X. He, G.D. Doolen, Thermodynamic foundations of kinetic theory and lattice Boltzmann models for multiphase flows, J. Stat. Phys. 107 (2002) 309–328. https://doi.org/10.1023/A:1014527108336
[28] N.S. Martys, X. Shan, H. Chen, Evaluation of the external force term in the discrete boltzmann equation, Phys. Rev. E 58 (1998) 6855–6857. https://doi.org/10.1103/PhysRevE.58.6855
[29] X. Shan, X. Yuan, H. Chen, Kinetic theory representation of hydrodynamics: a way beyond the Navier-Stokes equation, J. Fluid Mech. 550 (2006) 413–441. https://doi.org/10.1017/S0022112005008153
[30] Z. Li, X. Shan, Body-force modelling in thermal compressible flows with the lattice Boltzmann method, J. Fluid Mech. 964 (2023). https://doi.org/10.1017/jfm.2023.328
[31] X. Li, Z. Li, W. Duan, X. Shan, Self-consistent force scheme in the spectral multiple-relaxation-time lattice Boltzmann model, Phys. Rev. E 109 (2024) 15301. https://doi.org/10.1103/PhysRevE.109.015301
[32] G.-Q. Chen, A.-M. Zhang, X. Huang, On the interaction between bubbles and the free surface with high density ratio 3D lattice Boltzmann method, Theor. Appl. Mech. Lett. 8 (4) (2018) 252–256. https://doi.org/10.1016/j.taml.2018.04.006
[33] T. Xiao, Q. Cai, K. Xu, A well-balanced unified gas-kinetic scheme for multiscale flow transport under gravitational field, J. Comput. Phys. 332 (2017) 475–491. https://doi.org/10.1016/j.jcp.2016.12.022
[34] H. Grad, On the kinetic theory of rarefied gases, Commun. Pure Appl. Math. 2 (4) (1949) 331–407. https://doi.org/10.1002/cpa.3160020403
[35] B.T. Nadiga, D.I. Pullin, A method for near-equilibrium discrete-velocity gas flows, J. Comput. Phys. 112 (1) (1994) 162–172. https://doi.org/10.1006/jcph.1994.1089
[36] C. Coreixas, J. Latt, Compressible lattice Boltzmann methods with adaptive velocity stencils: an interpolation-free formulation, Phys. Fluids 32 (11) (2020) 116102. https://doi.org/10.1063/5.0027986
[37] Z. Li, Improved gas kinetic flux solver with locally rescaled Gauss-Hermite quadrature for supersonic continuum and rarefied flows, J. Comput. Phys. 524 (2025) 113700. https://doi.org/10.1016/j.jcp.2024.113700
[38] A. Frezzotti, P. Barbante, L. Gibelli, Direct simulation Monte Carlo applications to liquid-vapor flows, Phys. Fluids 31 (6) (2019) 62103. https://doi.org/10.1063/1.5097738
[39] R. Huang, Mesoscopic perspectives on dynamic van der Waals theory for liquid-vapor phase transition, Phys. Fluids 34 (12) (2022). https://doi.org/10.1063/5.0132865
[40] J.H. Ferziger, H.G. Kaper, E.P. Gross, Mathematical theory of transport processes in gases, Am. J. Phys. 41 (4) (1973) 601–603. https://doi.org/10.1119/1.1987312
[41] T. Chen, C. Zhang, L.-P. Wang, Diffuse interface model for a single-component liquid-vapor system, Phys. Rev. E 107 (2023) 25104. https://doi.org/10.1103/PhysRevE.107.025104
[42] A. Frezzotti, L. Gibelli, S. Lorenzani, Mean field kinetic theory description of evaporation of a fluid into vacuum, Phys. Fluids 17 (1) (2004) 12102. https://doi.org/10.1063/1.1824111
[43] H. Grad, Note on n-dimensional Hermite polynomials, Commun. Pure Appl. Math. 2 (4) (1949) 325–330. https://doi.org/10.1002/cpa.3160020402
[44] X. Shan, Central-moment-based Galilean-invariant multiple-relaxation-time collision model, Phys. Rev. E 100 (2019) 43308. https://doi.org/10.1103/PhysRevE.100.043308
[45] Z. Cai, M. Torrilhon, On the Holway-Weiss debate: convergence of the Grad-moment-expansion in kinetic gas theory, Phys. Fluids 31 (12) (2019) 126105. https://doi.org/10.1063/1.5127114
[46] S. Yan, X. Shan, Lattice Boltzmann simulation of nonequilibrium flows using spectral multiple-relaxation-time collision model, AIAA J. 62 (12) (2024) 4518–4532. https://doi.org/10.2514/1.J063970
[47] V.E. Ambruș, V. Sofonea, Lattice Boltzmann models based on half-range Gauss-Hermite quadratures, J. Comput. Phys. 316 (2016) 760–788. https://doi.org/10.1016/j.jcp.2016.04.010
[48] Y. Shi, Comparison of different Gaussian quadrature rules for lattice Boltzmann simulations of noncontinuum Couette flows: From the slip to free molecular flow regimes, Phys. Fluids 35 (7) 72015. https://doi.org/10.1063/5.0158713
[49] L. Luo, S. Tian, L. Wu, Multiscale simulation of interacting turbulent and rarefied gas flows in the dsmc framework, Theor. Appl. Mech. Lett. 15 (5) (2025) 100606. https://doi.org/10.1016/j.taml.2025.100606
[50] W. Su, L. Zhu, P. Wang, Y. Zhang, L. Wu, Can we find steady-state solutions to multiscale rarefied gas flows within dozens of iterations, J. Comput. Phys. 407 (2020) 109245. https://doi.org/10.1016/j.jcp.2020.109245
[51] Z. Shi, Y. Zhang, L. Wu, General synthetic iterative scheme for non-equilibrium dense gas flows, J. Comput. Phys. 520 (2025) 113501. https://doi.org/10.1016/j.jcp.2024.113501
[52] A. Frezzotti, L. Gibelli, D.A. Lockerby, J.E. Sprittles, Mean-field kinetic theory approach to evaporation of a binary liquid into vacuum, Phys. Rev. Fluids 3 (2018) 54001. https://doi.org/10.1103/PhysRevFluids.3.054001